Near-Surface Wind Convergence over the Gulf Stream—The Role of SST Revisited

R. J. SMALL,[a] V. ROUSSEAU,[b] R. PARFITT,[c] L. LAURINDO,[a,d] L. O'NEILL,[e] R. MASUNAGA,[f] N. SCHNEIDER,[g] AND P. CHANG[h]

[a] *Climate and Global Dynamics Laboratory, National Center for Atmospheric Research, Boulder, Colorado*
[b] *CECI, Université de Toulouse, CNRS, CERFACS, Toulouse, France*
[c] *Department of Earth Ocean and Atmospheric Science, Florida State University, Tallahassee, Florida*
[d] *Cooperative Institute for Marine and Atmospheric Studies, University of Miami, Miami, Florida*
[e] *College of Earth, Ocean, and Atmospheric Sciences, Oregon State University, Corvallis, Oregon*
[f] *Japan Agency for Marine-Earth Science and Technology, Yokohama, Kanagawa, Japan*
[g] *Department of Oceanography and International Pacific Research Center, University of Hawai'i at Mānoa, Honolulu, Hawaii*
[h] *Department of Oceanography, Texas A&M University, College Station, Texas*

(Manuscript received 16 June 2022, in final form 6 April 2023, accepted 10 April 2023)

ABSTRACT: High-resolution observations have demonstrated the presence of strong time-mean near-surface wind convergence (NSWC) anchored across oceanic frontal zones, such as the western boundary currents. Initial analyses appeared to show a close association between this time-mean NSWC and time-mean properties of the underlying sea surface temperature (SST), such as the gradients and second derivatives (e.g., Laplacian of SST), acting through pressure-adjustment and vertical-mixing mechanisms. However, a series of recent papers have revealed the instantaneous NSWC to be dominated by atmospheric fronts and have suggested the importance of air–sea processes occurring instead on shorter, synoptic time scales. In this paper, using the ERA5 reanalysis dataset in the Gulf Stream region, we aim to reconcile these viewpoints by investigating the spatial and temporal dependence of NSWC and its relationship to SST. It is revealed that while atmospheric frontal processes govern the day-to-day variability of NSWC, the relatively weak but persistent pressure-adjustment and vertical-mixing mechanisms provide lower-frequency modulations in conditions both with and without atmospheric fronts. In addition to their temporal characteristics, each mechanism is shown through spectral analysis to dominate on specific spatial scales. In light of recent work that has tied remote atmospheric responses to NSWC anomalies in western boundary current regions, these results emphasize the importance of oceanic frontal zones for atmospheric variability on all spatiotemporal scales.

KEYWORDS: Atmosphere–ocean interaction; Boundary currents; Fronts; Boundary layer

1. Introduction

This paper addresses near-surface convergence and associated quantities over a region of the extratropical ocean, revisiting proposed linkages to SST. Whereas theories for the response of surface convergence and precipitation to tropical SST have been available for many decades (e.g., Matsuno 1966; Gill 1980; Lindzen and Nigam 1987; Stevens et al. 2002; Sobel and Neelin 2006; Back and Bretherton 2009; Maloney 2009; de Szoeke and Maloney 2020; Duffy et al. 2020), theories for extratropical response to SST have been slower to emerge, and numerical and observational results are often hard to interpret because of the compounding influence of weather "noise" (reviewed in Kushnir et al. 2002; Czaja et al. 2019; Seo et al. 2022).

Despite this, the possibility of a deep response to extratropical SST was raised by Minobe et al. (2008), who identified near-surface convergence and strong vertical motion throughout the troposphere, high frequency of deep cloud, and precipitation over the warm Gulf Stream current, and similar findings were found for the Kuroshio Extension (Tokinaga et al. 2009). A consequent far-reaching, downstream response (e.g., via large scale Rossby waves) has also been discussed (Hand et al. 2014; Wills et al. 2016; Lee et al. 2018; Siqueira and Kirtman 2016). Minobe et al. (2008) hypothesized that the deep motion resulted from a response of the atmosphere to SST, via the so-called pressure-adjustment mechanism, which links SST to sea level pressure (SLP) via warming and

Supplemental information related to this paper is available at the Journals Online website: https://doi.org/10.1175/JCLI-D-22-0441.s1.

Rousseau's current affiliation: MAGELLIUM, Ramonville Saint-Agne, France.

Corresponding author: R. Justin Small, jsmall@ucar.edu

DOI: 10.1175/JCLI-D-22-0441.1

moistening of the boundary layer. This was inferred from a spatial resemblance between the following fields: Laplacian of SST, negated ($-\nabla^2$SST; hereafter the ∇^2 symbol is used for references to Laplacians), ∇^2SLP, near-surface wind convergence (referred to here as NSWC), and precipitation. This was seen for long-term annual means in satellite and reanalysis data. The hypothesis was expanded upon by Minobe et al. (2010), Kuwano-Yoshida et al. (2010), and Takatama et al. (2015), with apparent confirmation from satellite data of interior air temperature by Shimada and Minobe (2011). The Minobe et al. (2008) hypothesis was related to earlier theoretical work on boundary layer–free troposphere coupling by Feliks et al. (2004, 2007), who explored the impact of vertical motion driven by ∇^2SST on a quasigeostrophic free troposphere. (The latter papers also suggested the presence of an upper tropospheric jet roughly parallel to the ocean front.)

Another process driving wind response to mesoscale SST is the vertical-mixing mechanism (Hayes et al. 1989; Xie et al. 1998; Chelton et al. 2001) by which surface wind speed is increased (decreased) over warm (cold) SST due to turbulent momentum fluxes acting on an upper boundary layer jet. Evidence of this mechanism being active over the Gulf Stream has been presented in Chelton et al. (2004) and O'Neill et al. (2017). Response times for this process and the pressure-adjustment mechanism are expected to be short, a few hours to a day, to affect the boundary layer structure (Schneider and Qiu 2015; Seo et al. 2022).

Since the work of Minobe et al. (2008), it has been recognized that different processes shape the synoptic-time-scale atmosphere response to the Gulf Stream than for the long-term mean, and the importance of the pressure-adjustment mechanism has been questioned. Perhaps the first paper to expand on the Minobe results was Brachet et al. (2012), who separated sub-10 day and longer time scales and found different processes dominating the response in SLP. Specifically, they separated the Laplacian of SLP (∇^2SLP) into two components:

$$\nabla^2\mathrm{SLP} = a\zeta_{850} - b\nabla^2 T_{\mathrm{BL}}, \tag{1}$$

where T_{BL} is the temperature in the boundary layer and ζ_{850} is the geostrophic vorticity at 850 hPa, and a and b are constants (derived from Feliks et al. 2004, 2007). Using an atmospheric general circulation model with a relatively fine atmosphere grid of around 50 km, they found that the boundary layer temperature component [second term on the right-hand side of Eq. (1)] dominates at long time scales, but at short time scales, the geostrophic vorticity due to synoptic variability [first term on the right-hand side of Eq. (1)] dominates. The pressure-adjustment mechanism has also been shown to operate on periods as short as 2–3 weeks by Nelson and He (2012).

Subsequently, a series of papers examined the Minobe et al. (2008) hypothesis in more detail, focusing on the role of synoptic transients. Parfitt and Czaja (2016) noted that the time-mean vertical motion field was not a typical state of the atmosphere over the Gulf Stream, and at any given time, the vertical motion is dominated entirely by the strong upward and downward motions associated with synoptic weather. Meanwhile, O'Neill et al. (2017) showed that the pressure-adjustment model cannot explain the daily occurrence of these surface convergences or divergences, since, on rain-free days, there is dominant surface divergence even though the Laplacian of SST field would indicate NSWC via the pressure-adjustment mechanism. Further, from analysis of daily data, there was found to be negligible sensitivity of the sign of the surface divergence field to the sign of ∇^2SST. Results presented on the relationship of ∇^2SST to the divergence field in the presence of rain were debated by Plougonven et al. (2018) and O'Neill et al. (2018).

O'Neill et al. (2017) further propose that NSWC (and precipitation) over the Gulf Stream is due to the collocation of the midlatitude storm track and the Gulf Stream (Hoskins and Hodges 2002; Booth et al. 2010), with NSWC occurring when wind flows from warm water toward cold (i.e., toward the north if the Gulf Stream was oriented zonally after separating from the coast) and generally associated with synoptic storms. Parfitt and Seo (2018) went further to suggest that the time-mean surface convergence is actually a residual of atmospheric fronts, embedded within the synoptic storms, and illustrated that their removal from the time-mean results in only weak divergence. A possible interpretation of this series of papers is that the time-average boundary layer response due to pressure adjustment is unimportant to convergence over the Gulf Stream.

The main hypothesis of this new work is that the NSWC is a combination of internal atmospheric dynamic processes (such as fronts), as well as SST–boundary layer effects, with these processes dominating in different parts of wavenumber–frequency space. Note that this is different from the conclusions of some of the papers reviewed above, which tended to attribute the NSWC exclusively to just one of the mechanisms. It can, however, be considered an expansion upon Brachet et al. (2012), who identified the joint importance of synoptic variability and boundary layer processes.

Thus, the aim of the paper is to reconcile and quantify all the various proposed mechanisms for Gulf Stream NSWC, and to investigate the time- and space-scale dependence of mechanisms. The novelty of this work is that we will use a variety of diagnostics and metrics to assess the role of each process that has been proposed, including whether they can work concurrently, or at different scales. This should enable us to synthesize previous findings. After describing the methods and data in section 2, time variability is discussed in section 3, followed by an interpretation of the time mean in section 4 and presentation of the vertical structure and precipitation in section 5, and finally, discussion and conclusions. The focus is on the winter season, and December in particular, when synoptic variability is strong, but note that the long time series analysis of section 3 uses data from all months of the year.

2. Methods and data

a. Datasets

The state-of-the-art atmosphere reanalysis ERA5 (Hersbach et al. 2020) is used here due to its use of observational data, dynamical consistency, and high resolution. ERA5 has a fine

model grid spacing of 31 km (spectral TL639), and 137 levels in the atmosphere. Data assimilation is a 4D VAR ensemble. Among the many datasets ingested are satellite scatterometer near-surface winds. Prior to September 2007, the boundary SST is from HadISST2.1.0.0 on a 0.25° grid, and afterward from the Operational Sea Surface Temperature and Sea Ice Analysis (OSTIA) (0.05° grid; Donlon et al. 2007). ERA5 uses an upgraded Tiedtke (1989) scheme to parameterize convection. The methods described below are applied to hourly ERA5 data with derived statistics such as monthly mean and monthly median. A 0.25° gridded version of ERA5 is used.

It may be questioned whether ERA5 can resolve the features of interest in this study, since, for example, atmosphere fronts have cross-front scales of ~100 km and ocean eddies can have scales below 100 km, both of which will only be "permitted" by an atmosphere model with the grid size of ERA5. However, we found that atmosphere fronts are well represented (Fig. S1 in the online supplemental material) and mesoscale boundary layer effects are also clear (Fig. S2) compared to satellite data such as the Quick Scatterometer (QuikSCAT) dataset and the Cross-Calibrated Multi-Platform dataset [CCMPv3; earlier versions are described in Atlas et al. (2011) and Mears et al. (2019)]. This suggests that the assimilation of datasets, especially satellite scatterometry, is helping to represent the features of interest that would otherwise be only partly resolved by a free-running model. However, despite the qualitative agreement between ERA5 and QuikSCAT in the cases shown in Figs S1 and S2, a more thorough comparison performed in Masunaga and Schneider (2022) for daily data from 2003 to 2008 revealed that ERA5 underestimated the wind response to SST by 20%–30% on average.

b. *Analyzing the SST influence across different spatial and temporal scales*

The main tool used for assessing variability and covariability in this paper is spectral analysis in wavenumber and frequency space. This method allows one to identify the key scales in time and space where signals are strong and/or related. In contrast, other methods such as time–domain correlations essentially average over all frequencies and will not clearly show the effect of a covariability between variables occurring in a narrow range of frequencies. (It is similar for spatial correlations that average over all wavenumbers.) The spectral approach avoids the requirement for prefiltering to show signals of interest via correlation.

To infer the influence of SST fronts in the NSWC across different spatial and temporal scales, we contrast zonal–temporal (Hovmöller) diagrams of the considered quantities for zonal sections. The Hovmöller diagrams are also used to compute the cross-spectral statistics such as the magnitude-squared coherency (γ^2_{XY}) and phase factor (θ_{XY}) between the mentioned quantities as a function of both zonal wavenumber and frequency, to analyze how they are linearly related over scales between about 40 and 5000 km and between 2 h and 15 months.

For the spectral analysis of section 3c, we define anomalies by removing the zonal average from 74° to 10°W, and further remove the long-term mean, the linear trend, and the seasonal cycle at each point (composed of annual and semiannual components). For this, a time record of the period 1979–2018 is used, for latitude 40°N, which passes through the band of time-mean convergence over the Gulf Stream (Minobe et al. 2008), and a zonal extent from about 74° to 10°W, which spans the Atlantic. (The full Atlantic width allows for analysis of longer signals than if only the western boundary were used.) Data from all calendar months are used. The resulting anomaly diagrams are then subdivided into approximately 17.5-month-long segments with a 50% temporal overlap, which are then Fourier transformed to obtain an ensemble containing 54 realizations of the spectrum of each quantity. These are used to compute the power spectral density of each quantity, and the cross-spectral density between pairs of quantities, defined following Bendat and Piersol (1986) as

$$G_{XX}(k,\omega) = \frac{2}{LT}\langle|\tilde{X}(k,\omega)|^2\rangle,$$

$$G_{YY}(k,\omega) = \frac{2}{LT}\langle|\tilde{Y}(k,\omega)|^2\rangle, \quad \text{and}$$

$$G_{XY}(k,\omega) = \frac{2}{LT}\langle\tilde{X}^*(k,\omega)\tilde{Y}(k,\omega)\rangle,$$

where G_{XX} and G_{YY} are the power spectral densities of the signals X and Y, and G_{XY} is their cross-spectrum, the tilde indicates the Fourier transform to the zonal wavenumber and frequency domains (k and ω, respectively), L and T refer to the length of the zonal wavenumber and frequency domains, respectively, and the angle brackets represent ensemble averages over the 54 realizations of the enclosed quantities. Here, the phase factor θ_{XY} is defined as the phase of the cross-spectrum, where $G_{XY} = |G_{XY}|\exp(-i\theta_{XY})$.

Using the spectra above, the squared coherency can be computed as

$$\gamma^2_{XY} = \frac{|G_{XY}|^2}{G_{XX}G_{YY}}.$$

The squared coherency varies from zero to one and measures the fraction of the variance in signal Y that can be explained by X at a given spectral coordinate. In turn, the phase factor shows the phase relationship between two signals, with absolute angles equal to 0° indicating that fluctuations in X and Y more frequently display the same sign, equal to 90° indicating that the signals are in quadrature with each other, and equal to 180° indicating that fluctuations in each signal more frequently show opposite signs. Note that, as the phase speed $c = \omega/k$ links time and space variations, two highly coherent signals at a specific zonal wavenumber and frequency will have the same phase speed. For the 90° phase case, this means that one variable is spatially located one-quarter wavelength from the other, and the time difference of their peaks, that is, lag in time, is 1/4 time period.

c. *Supporting methods and illustrations*

1) BOUNDARY LAYER METRICS

This paper also uses metrics that are well established in the literature as providing insight on boundary layer and frontal

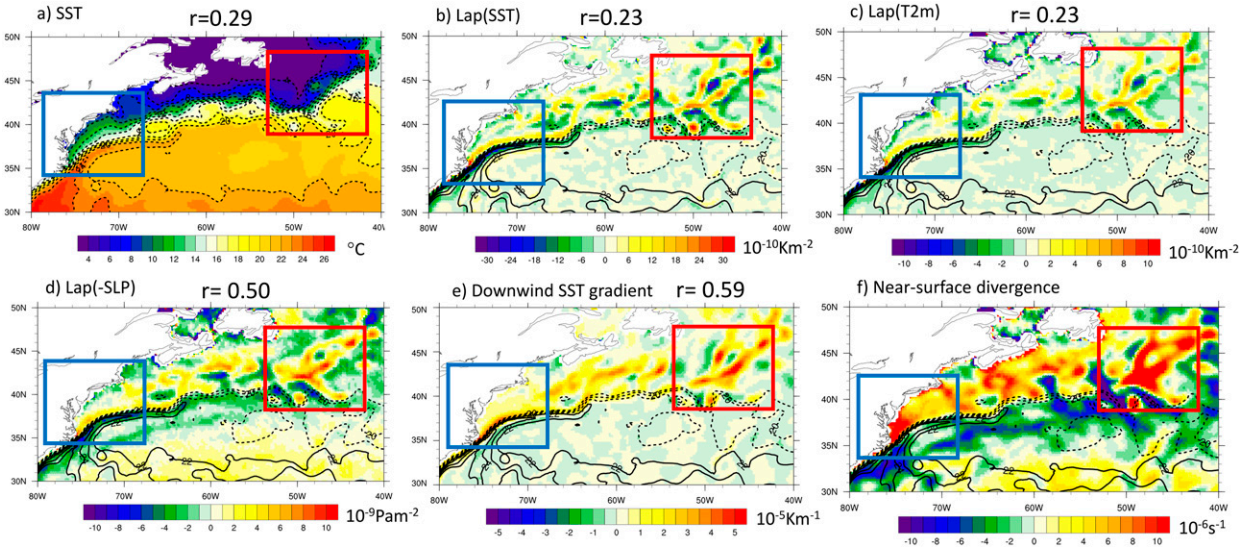

FIG. 1. One-month average fields for December 2018. (a) SST (shading and contours), (b) Laplacian (SST), (c) Laplacian (T2m), (d) Laplacian of sign-reversed SLP, (e) downwind SST gradient, and (f) near-surface wind divergence field, all from ERA5. Data have been smoothed with a 9-point local 2D smoother for plotting. In (b)–(f) SST(°C) contours are added: 22°, 23°, 24°, and 25°C (all solid) show the Gulf Stream warm core; 19°, 20°, and 21°C (dashed) indicate a single front of temperature, with some meandering and eddies, see (a). For (a)–(e), the pattern correlation r with near-surface divergence is indicated in the title. Note that Fig. S3 shows these fields without contour overlay, as the contours can obscure the shaded field.

processes: the divergence field at 10 m, referred to here as the near-surface divergence field (e.g., Chelton et al. 2001), ∇^2SST, the Laplacian of air temperature at 2 m (referred to as T2m, so ∇^2T2m) and of SLP (∇^2SLP; Lindzen and Nigam 1987; Feliks et al. 2004, 2007; Minobe et al. 2008), and downwind SST gradient (e.g., Chelton et al. 2001; O'Neill et al. 2003). Further, the divergence field and vertical motion at different vertical levels in the boundary layer and free troposphere are investigated. Note that in this paper, "divergence field" refers to the whole field including regions of different sign (i.e., convergences and divergences), whereas specific cases of one-signed "convergence" (such as NSWC) or "divergence" are referred to without use of the word "field."

2) ATMOSPHERE FRONT METRICS

Instantaneous snapshots are also used for illustration, incorporating atmospheric frontal masking. Surface atmospheric fronts are objectively identified in this study at 900 hPa, as recommended by Hewson (1998), using the "F" diagnostic or "T" diagnostic (Parfitt et al. 2017). The F diagnostic is defined as the product of the horizontal temperature gradient ∇T and relative vorticity ζ, normalized by the Coriolis parameter f at the relevant latitude and a typical horizontal temperature gradient, that is, $F = |\nabla T|\zeta/(f|\nabla T|_o)$. It is noted that this particular combination of variables is known to aid specifically in the identification of the associated frontal rainband (Solman and Orlanski 2010) and is thus ideally suited for this analysis. In addition, a minimum length criterion on each atmospheric front of 500 km is imposed. In contrast, the T diagnostic is derived purely from a function of temperature gradients (Hewson 1998).

For some spatial maps presented in this manuscript, we employ correlation methods (Pearson's correlation coefficient) in space to make an assessment of two fields in terms of one single number (also known as pattern correlation).

In section 4, a spatial filter is applied to the divergence field, which uses a box-car filter of full-width 5°, with land points excluded.

3. Variability of the divergence field in time and space

a. *Case studies from December 2018*

We start by illustrating the contrasting pictures that emerge from viewing time-averaged data (monthly here) compared with instantaneous data from December 2018. Starting with the monthly mean case (Fig. 1), the SST field shows the warm core of the Gulf Stream separating from the coast at Cape Hatteras (blue box in Fig. 1a) and heading east; farther downstream, the flow, which now has a less well-defined core, meanders and then turns northeastward (red box in Fig. 1a). Signatures of mesoscale eddies and filaments can be seen more clearly in the ∇^2SST field (e.g., red box in Fig. 1b), and similar spatial structures in this region are seen in other fields (Figs. 1c–f). It is notable that some features in the divergence field (Fig. 1f) relate to ∇^2SST (Fig. 1b) and to ∇^2T2m (Fig. 1c) (such as in the red box in Fig. 1), but not all (e.g., in the blue box of Fig. 1, the NSWC over the Gulf Stream is much broader than the negative ∇^2T2m and ∇^2SST). Meanwhile, ∇^2T2m is very similar in spatial pattern to ∇^2SST but has a reduced amplitude. The pattern correlation r between the near-surface divergence field and the various other fields for the domain of Fig. 1 is shown in the panel titles. Both for ∇^2SST

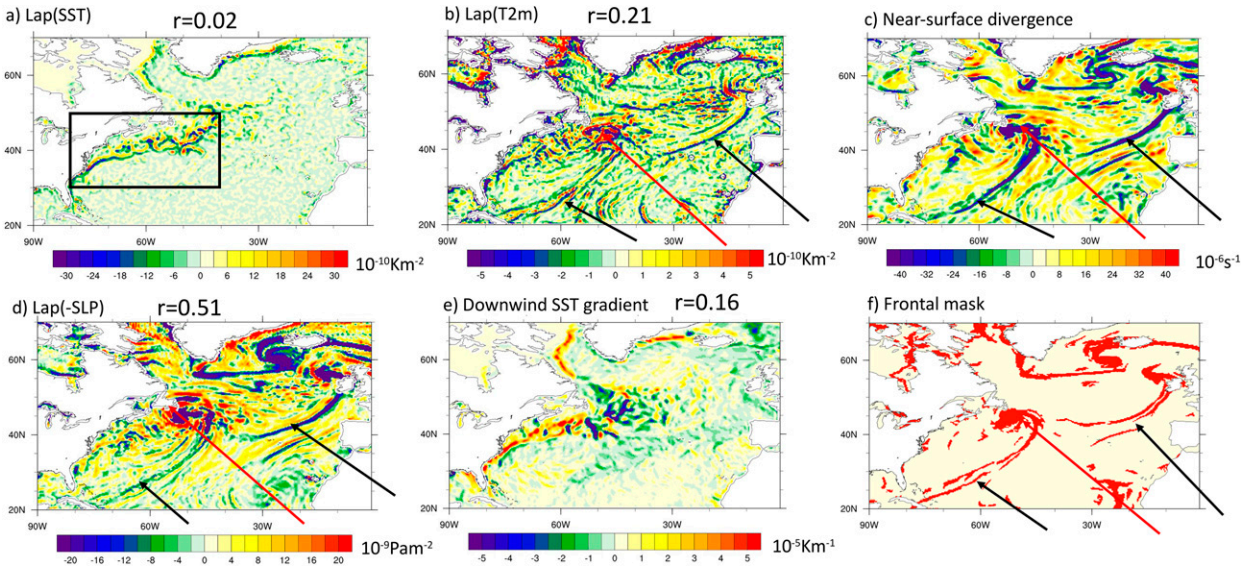

FIG. 2. Hourly snapshot from December 2018 (0000 UTC 7 Dec 2018). (a) Laplacian (SST), (b) Laplacian (T2m), (c) near-surface wind divergence, (d) Laplacian of sign-reversed SLP, and (e) downwind SST gradient, all from ERA5. (f) Atmosphere frontal masks are shown for the same time stamp [red indicates presence of a front according to the F diagnostic of section 2c(2)]. Arrows point to atmosphere front signatures. For (a), (b), (d), and (e), the pattern correlation r with near-surface divergence is indicated in the title. The box in (a) shows the domain used for Fig. 1.

and ∇^2T2m, $r = 0.23$. The pattern of sign-reversed ∇^2SLP is similar to that of the divergence field ($r = 0.5$). The downwind SST gradient also shows similar structures to ∇^2T2m and to the near-surface wind divergence field ($r = 0.59$), although the downwind SST gradient is more positive signed, which would encourage wind divergence under the standard vertical-mixing argument (Chelton et al. 2001). Thus, consistent with previous work (Minobe et al. 2008), monthly mean fields partly show the influence of mesoscale ocean structure on the divergence field. It is worth noting, however, that many features in the divergence field do not have an obvious correspondence with ∇^2SST or the downwind SST gradient, such as in the region south of the SST front between 75° and 55°W where there is strong convergence but the SST gradients are very weak.

In general, features in the divergence field appear to be broader than those in ∇^2SST, ∇^2T2m, and the downwind SST gradient, which may be due to advection processes in the atmosphere boundary layer smoothing out the surface signal but could also be due to the influence of other processes, such as atmosphere fronts (see section 4).

An instantaneous snapshot from 7 December 2018 (Fig. 2) shows characteristics very different from the monthly mean. The date and time were chosen to illustrate typical conditions in winter, with long atmosphere fronts in the North Atlantic associated with synoptic storms. A larger domain is shown in Fig. 2 to illustrate the synoptic context. For reference, the near-surface wind divergence field is shown (Fig. 2c) and a frontal mask [Fig. 2f; using the F diagnostic of Parfitt et al. (2017)]. The ∇^2T2m (Fig. 2b) shows structures also seen in the divergence field (i.e., the atmosphere fronts; see black arrows and red arrows), and the pattern correlation over this large domain is $r = 0.21$. The divergence field and ∇^2SST have no obvious spatial relationship in this instantaneous view ($r = 0.02$). This is consistent with the finding from O'Neill et al. (2017), based on conditional analysis of high-frequency data, that the sign of ∇^2SST did not determine the sign of near-surface divergence. Sign-reversed ∇^2SLP (Fig. 2d) also shows atmosphere front signatures ($r = 0.51$). Meanwhile, the downwind SST gradient (Fig. 2e) shows maximum magnitude in the ocean front region, as expected, and also shows wide bands of alternating sign that likely correspond to changing wind direction in sectors of storms. Its pattern correlation with near-surface divergence is $r = 0.16$.

More detail on the instantaneous fields in Fig. 2 is provided in the close-up Fig. S4, which covers the smaller domain of Fig. 1. This reveals that in addition to showing atmosphere front signatures, ∇^2T2m has hints of a spatial structure similar to ∇^2SST in parts of the domain, but not as obvious as in the monthly mean.

These two examples (monthly average and snapshot) confirm the findings of Minobe et al. (2008) that NSWC is related to mesoscale SST on long-term averages, but also confirm the finding of O'Neill et al. (2017) and Parfitt and Seo (2018) that the instantaneous or high-frequency view is dominated by extremes occurring in atmospheric systems. The strong relationship of fields like the divergence field and ∇^2T2m are clearly seen in animations of hourly data (see supplemental material) and also in the subsequent analysis. But what about the relationship of ∇^2SST to the divergence field in the monthly mean (Fig. 1) or longer time scales? Is this purely coincidental? This question is explored in section 4a below. In the remainder of

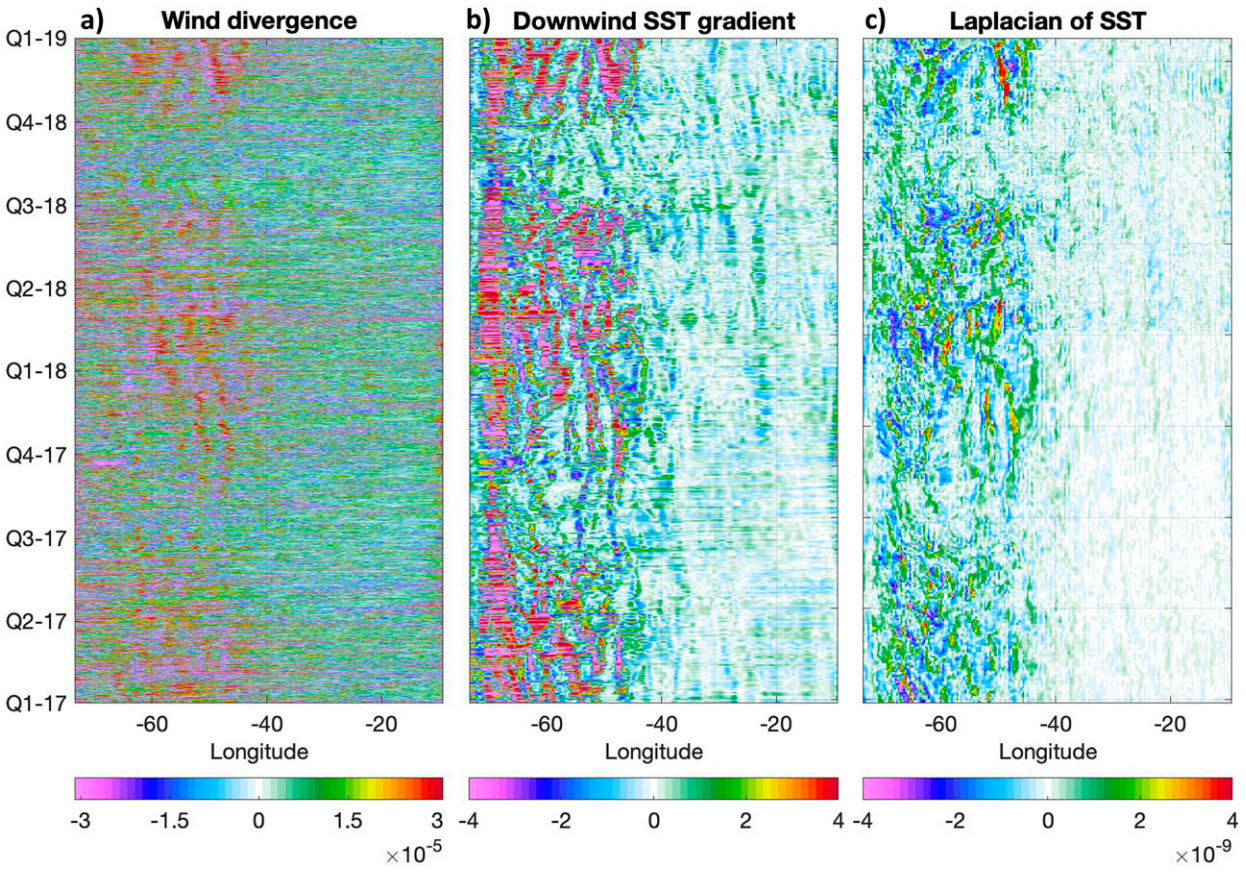

FIG. 3. Hovmöller at 40°N, showing two years of data, 2017 and 2018, labeled by quarter (Q1–Q4) and year. The data have the long-term trend and seasonal cycle removed but are otherwise unfiltered. (a) Near-surface wind divergence (10^{-5} s^{-1}). (b) Downwind SST gradient [K (100 km)$^{-1}$]. (c) Laplacian of SST (10^{-9} K m^{-2}).

this section, spatiotemporal variability of the divergence field and related fields is explored in more detail.

b. *Hovmöllers: Dependence on time scale*

Hovmöller diagrams at 40°N (Fig. 3) are next shown for a 2-yr segment (2017–18). Note that these data have the seasonal cycle and trend removed but are otherwise unfiltered. The near-surface wind divergence field is quite noisy, with a lot of high-frequency activity, as expected (Fig. 3a). Many synoptic and frontal effects appear as near-horizontal features, although there is also a hint of a slow modulation (near vertical striations in Fig. 3a). In contrast, the downwind SST gradient (Fig. 3b) and ∇^2SST (Fig. 3c) fields have a very different character from the divergence field, and are dominated by slower modulations focused on the western half of the domain (the ocean frontal region), which again appear as near-vertical striations.

A close-up for the month of December 2018 (Fig. 4) shows more detail of the wind divergence field variability. The synoptic and frontal effects appear now as propagating features in the divergence field, but close inspection reveals an underlying near-vertical feature in Fig. 4a. The downwind SST gradient (Fig. 4b) mostly comprises near-vertical stationary features in the western basin, but note that rapid changes in sign of these features occur due to changes in wind direction associated with atmosphere fronts. The downwind SST gradient does not have strong signals east of 40°W, contrasting with the bands of strong NSWC in the eastern domain. The ∇^2SST field (Fig. 4c) shows slow variability, while ∇^2T2m shows both the rapidly propagating features across the domain and near-vertical structure (Fig. 4d), thus combining the effects of atmosphere fronts and slower SST variability.

The slow modulations are seen more clearly in Hovmöller diagrams for two years of low-pass data [using a 10th-degree Butterworth filter with a half-power cutoff time scale at 30 days (Fig. 5)]. Now all fields show similar overall structure, including relatively stronger signals west of 40°W. The divergence field (Fig. 5a) still has remnants of the synoptic features (near horizontal), which are also hinted at in the downwind SST gradient. This is suggestive of atmosphere fronts leaving a residual when averaged over 30-day time scales, while the rest of the storm structure is removed with the time averaging. The divergence field shows more variability compared to the other fields in the eastern half of the domain (east of 40°W). ∇^2T2m shows features also seen in ∇^2SST and similar structures to the downwind SST gradient (Figs. 5b–d).

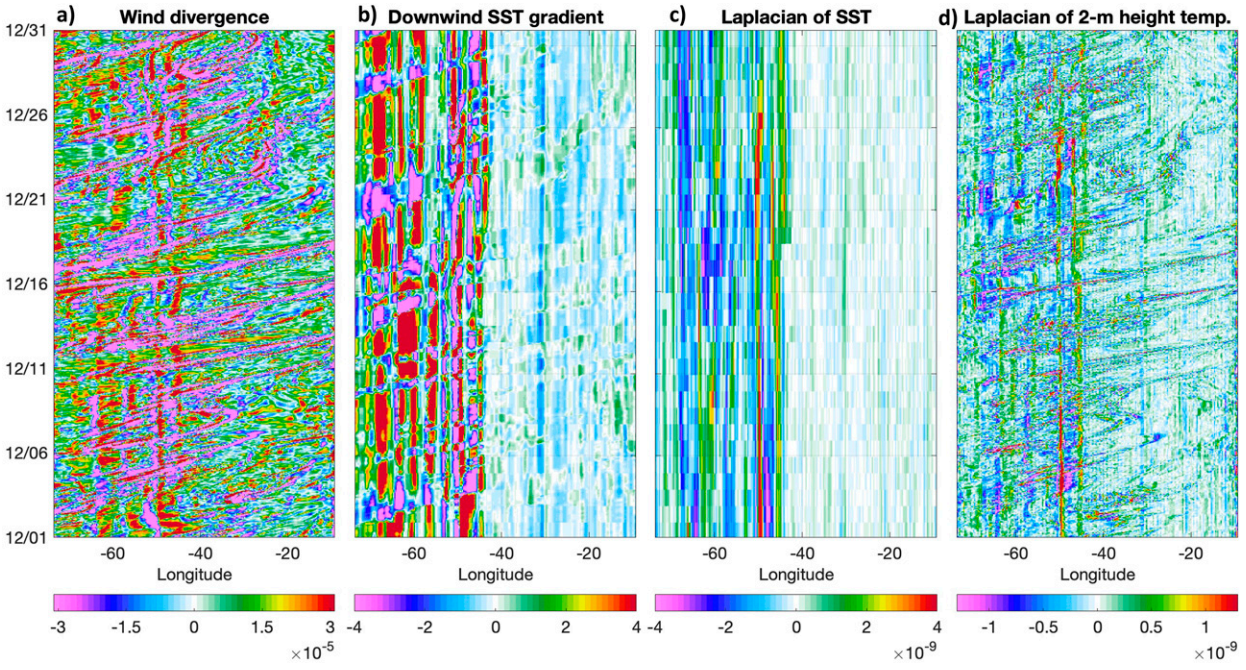

FIG. 4. As in Fig. 3, but a close up for December 2018. For reference, the Laplacian (T2m) is added in right panel (10^{-9} K m^{-2}).

c. *Wavenumber–frequency spectral analysis*

The previous illustrations of relationships between variables are now better quantified using wavenumber–frequency spectral analysis. This method is able to detect the time and space scales of covariability between pairs of variables of interest (Figs. 6 and 7). (The reader is reminded that all calendar months are used for this analysis, not just winter.) In general, robust signals are indicated by smoothly varying coherence and phase values in wavenumber–frequency space, while nonrobust signals typically appear with low coherence (e.g., white colors on top row of Figs. 6 and 7) and noisy phase relationships.

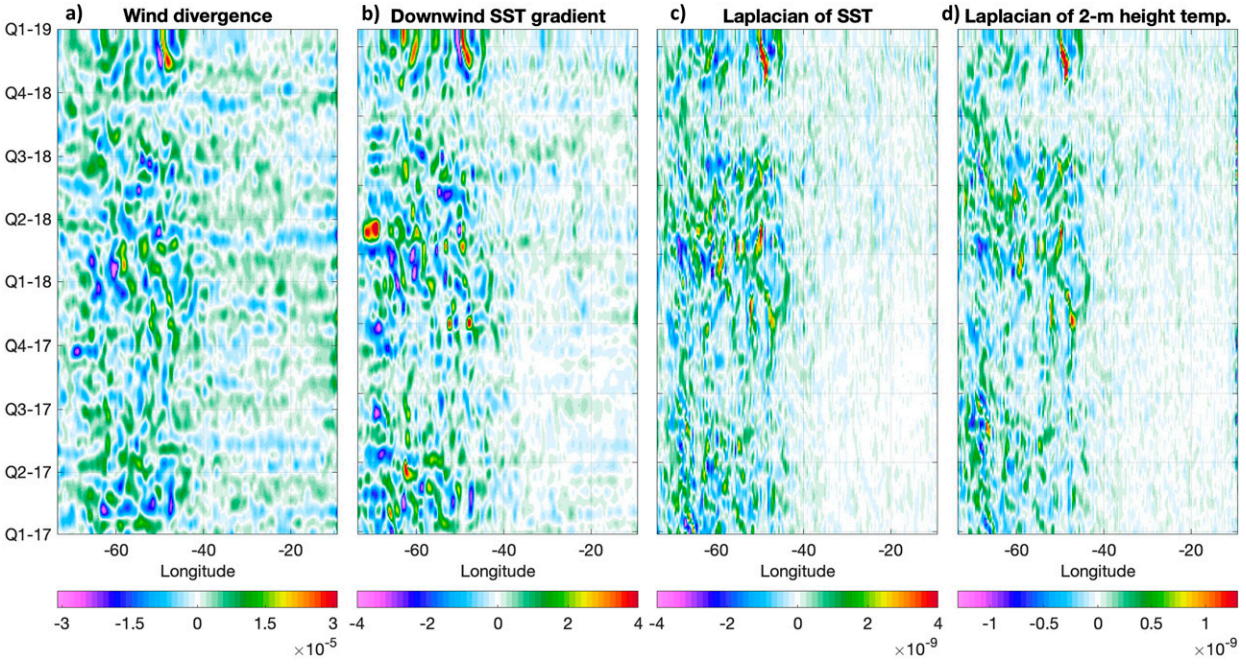

FIG. 5. As in Fig. 3, but for 30-day low-pass filtered data at 40°N, and with the Laplacian (T2m) added at right.

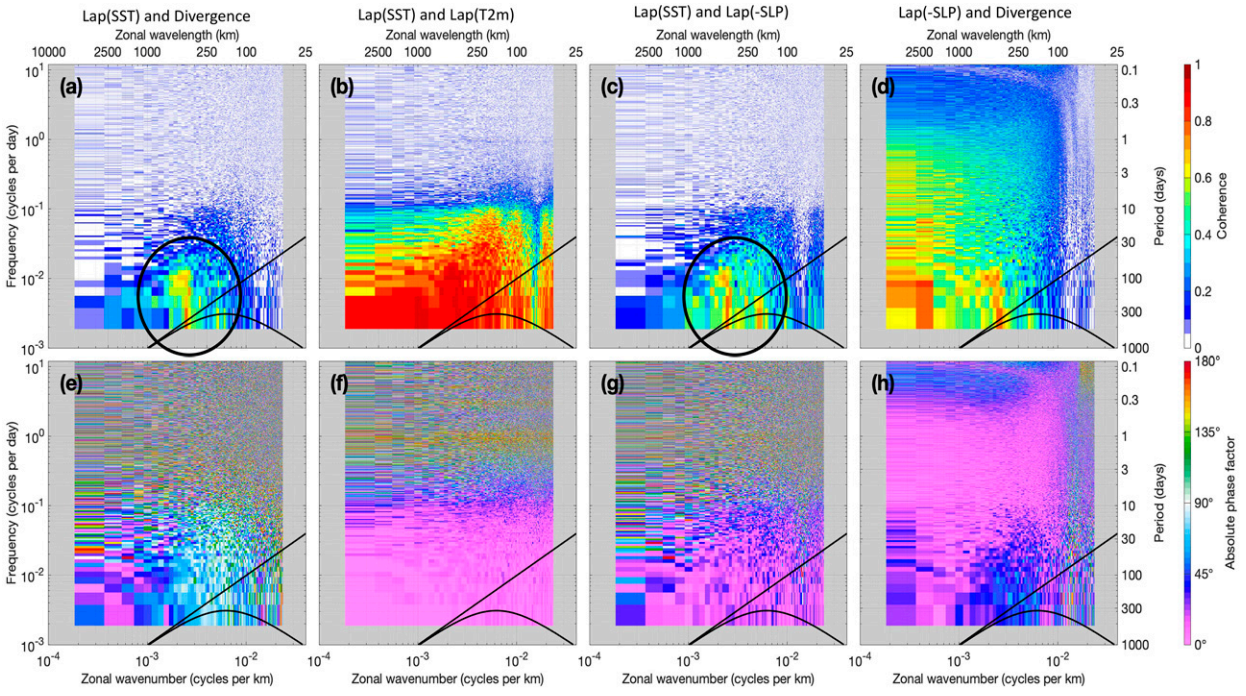

FIG. 6. Results of spectral coherence analysis in wavenumber and frequency space at 40°N. The pairs of variables being analyzed are labeled at the top of each column. Note that SLP is sign reversed as in Figs. 1 and 2. (top) Squared coherency (range from 0 to 1) and (bottom) the phase relationship (from 0° to 180°, with 0° implying in phase, 180° is out of phase). Axes show frequency (left axis) and period (right axis), and zonal wavenumber (bottom axis) and wavelength (top axis). In some panels, circles are used to highlight regions of enhanced coherence. The curved black line in each panel is the dispersion relations for oceanic, first-mode baroclinic Rossby waves. The straight black line marks the nondispersive wave limit.

The most robust relationship at all time scales is that between the near-surface wind divergence field and sign-reversed ∇^2SLP (Figs. 6d,h) with coherence at all except the shortest space scales (<100 km, which may be partly due to features at this scale being less well resolved by the ~31-km grid of ERA5). This robust relationship is represented both in Ekman dynamics (discussed in, e.g., Joyce et al. 2009; O'Neill et al. 2017) and also in the pressure-adjustment mechanism (Lindzen and Nigam 1987; Minobe et al. 2008) using Rayleigh friction.

For other pairs of variables, coherence is significant only in restricted regions of wavenumber–frequency space (Figs. 6 and 7). The ∇^2SST mainly affects other variables for time scales of 10 days or more. At these longer time scales, it is strongly coherent and in phase with ∇^2T2m over most spatial scales (Figs. 6b,f). In contrast, ∇^2SST only affects ∇^2SLP (Figs. 6c,g) and the near-surface divergence field (Figs. 6a,e) for a narrow range of spatial scales (~250–1000 km, corresponding approximately to ocean mesoscales) and is strongest for 30-day periods and longer. The phase relationship between ∇^2SST and the near-surface divergence field in this region is between 0° and 90°.

As expected from Figs. 1 and 2, and Figs. 4 and 5, ∇^2T2m is coherent with the near-surface divergence field and with ∇^2SLP, on time scales of 1 day or more, but most strongly for 30 days and more, particularly in the mesoscale ocean spatial scales (Figs. 7a,b,e,f). The phase relationship between ∇^2T2m and the near-surface divergence field in this region is close to 90° (Fig. 7e). Further, sign-reversed ∇^2SLP and the divergence field are about 45° phase related in this region, instead of the expected 0° (Fig. 6h). (The role of advection in the momentum equations may explain some of these lags.) The robust relationship between ∇^2SLP and ∇^2T2m (Figs. 7b,f) is indicative that either the temperature in the boundary layer is the dominant influence on SLP (at longer time scales) or that T2m is vertically coherent with the air temperature at upper levels (likely on shorter time scales, e.g., in atmosphere fronts).

The coherence between the downwind SST gradient and the divergence field is somewhat similar to that between ∇^2T2m and the divergence field, with larger values for time scales of 30 days and more, while the phase relationship for the former pair is nearer to 0° (Figs. 7c,g). This confirms and extends the finding from Fig. 1 that the three fields (divergence, downwind SST gradient, and ∇^2T2m) are related spatially on 30-day time scales. Meanwhile, ∇^2T2m and the downwind SST gradient are themselves closely linked (Figs. 7d,h), as shown by Foussard et al. (2019). At high wavenumbers and low frequency (e.g., ocean mesoscale), they are 90° out of phase, as can happen if ∇^2T2m overlies ∇^2SST (Foussard et al. 2019; e.g., in the special case of flow perpendicular to a linear ocean front). However, at higher frequencies (e.g., for 1–10 days), they are in phase. This may relate to T2m lagging SST under strong winds under the effect of thermal advection.

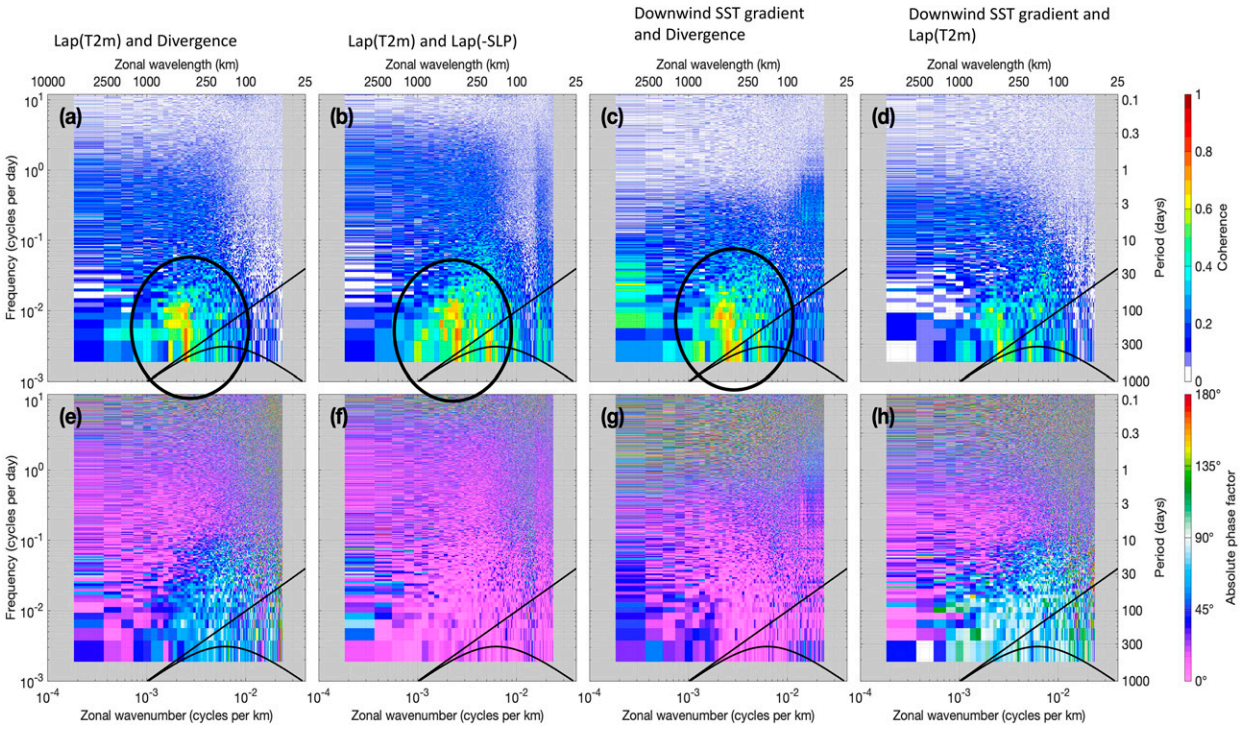

FIG. 7. As in Fig. 6, but for different pairs of variables, as labeled at the top of each column.

4. Decomposition and forcing of the time-mean divergence field

a. *Decomposition of time-mean divergence field*

The previous section focused on time and space variability, but some of its results are relevant to long-term time means. We present here a possible decomposition of the monthly mean near-surface divergence field and illustrate it in Fig. 8 for December 2018. The mean near-surface wind divergence field for that month is shown in Fig. 8f for reference. The decomposition is given as follows:

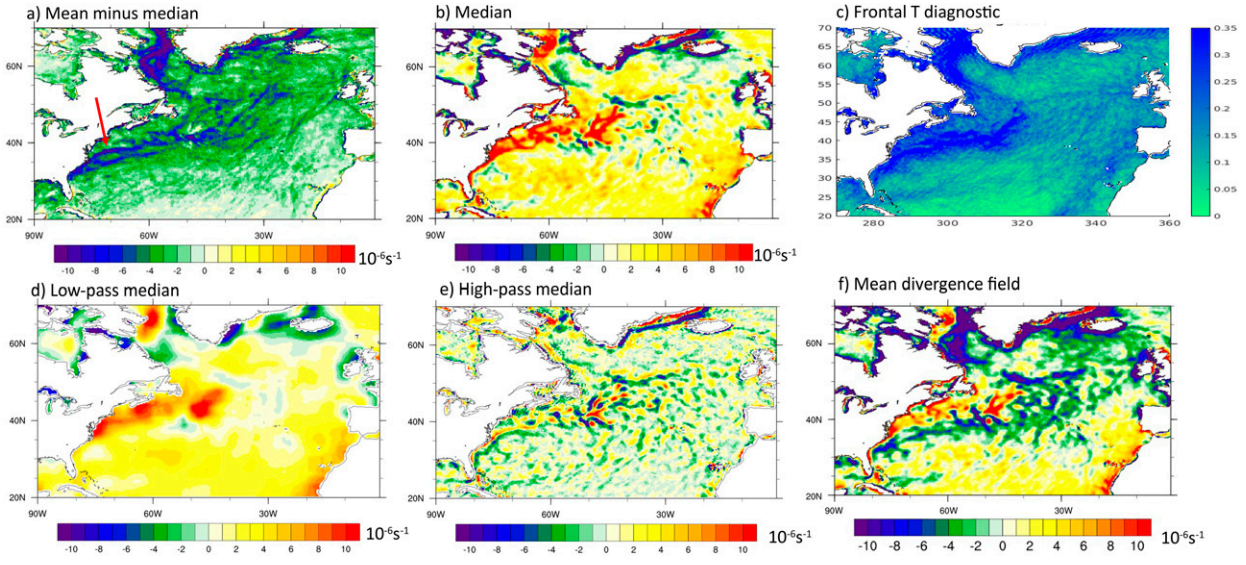

FIG. 8. A possible decomposition of the monthly mean near-surface wind divergence field for December (2018). (a) The difference between mean and median wind divergence for that month. (b) The median, (d) low-pass spatial filter of the median wind divergence field, and (e) high-pass spatial filter of the median. (c) The atmosphere frontal frequency (as a fraction of 1) using the T diagnostic is shown for comparison. (f) The mean near-surface divergence for the month. The arrowed feature in (a) is discussed in section 6c.

Time-mean divergence field = 1) NSWC due to large-amplitude high-frequency events, leaving an imprint in the mean + 2) large-scale divergence + 3) small-scale, boundary layer forced response to SST. This is not a traditionally defined decomposition but instead serves to indicate the major types of processes that drive the time mean. It may alternatively be written as 1) extremes + 2) large-scale residual + 3) small-scale residual, where here residual refers to the field excluding extremes.

Term 1: The NSWC due to large-amplitude high-frequency events is represented by the difference between the mean and median wind divergence field (Fig. 8a). [This simple metric was motivated by the analysis of O'Neill et al. (2017) showing large differences between the two statistics.] The field is almost exclusively negative, that is, indicating convergence, consistent with the strongly skewed nature of the divergence field (O'Neill et al. 2017). The field also shows a number of "streaks" and a clustering of features over the Gulf Stream (see also the corresponding field for December 2016, in Fig S5, which shows other notable examples of streaks). This appears to be a combination of storms and fronts propagating through the domain, and stationary fronts. In other words, these are the extreme, atmosphere frontal events that do not cancel out in the time mean, and they shift the mean toward negative values compared to the median (Parfitt and Czaja 2016; O'Neill et al. 2017). [There is some spatial similarity between the mean minus median metric and the frequency of atmosphere fronts as measured by the T diagnostic (section 2c) as seen in Fig. 8c; for comparison, the frequency as measured by the F diagnostic is shown in Fig. S6.] Note that viable alternatives to the simple "mean minus median" metric are, for example, two-standard-deviation events (O'Neill et al. 2017) or atmosphere front identifications (Parfitt et al. 2017).

The remaining contribution (the median, i.e., time mean minus term 1) is shown in Fig. 8b, and it can be further divided into two components, terms 2 and 3.

Term 2: The large-scale divergence field is represented by a low-pass spatial filter (see section 2c) of the median divergence field (Fig. 8d). In most of the region south of Greenland and to the west of the United Kingdom, the divergence field is positive, with an enhancement off the U.S. East Coast. As pointed out by O'Neill et al. (2017), the typical surface conditions in the region are divergent; indeed, much of the southern half of the geographical region shown in Fig. 8 is under the climatological subtropical high. For the region further north and under the midlatitude storm track, the divergence comes from intervals between cyclonic systems and fronts, for example, transient anticyclones. Note that the enhanced large-scale divergence off the U.S. East Coast may relate to the cold SST inshore of the Gulf Stream, or it could be a land–sea boundary effect. This aspect is not pursued further here.

Term 3: We hypothesize that the boundary layer–forced response to SST is represented by the high-pass spatial filter of the median divergence field (Fig. 8e). This field shows fine structures related to the ocean front, which will be considered in more detail in section 4b. Note that although bands of convergence are seen associated with the Gulf Stream in Fig. 8e, there are also regions of strong divergence. This makes the point that the boundary layer response is not causing the overall broad NSWC over the Gulf Stream and instead, it is modifying it with a fine-scale structure that in some regions will enhance convergence and in others will reduce convergence. (i.e., when term 1 and term 3 are summed).

The results above apply to a one-month mean; it may be asked if the long-term, multiyear mean is similar. We do not explicitly show a longer-term result here but can infer the expected result from the work of O'Neill et al. (2017), which analyzes the long-term mean and other statistics from 10 years of the QuikSCAT record. A similar decomposition to that above is shown in their Figs. 5 and 11. Specifically, they apply a filter to identify events that are larger in amplitude than two standard deviations (referred to as a 2σ filter) with a similar purpose to our mean minus median field. Thus identified, the contribution of their extremes is a reasonably broad region of NSWC centered on the Gulf Stream, while the residual is a large-scale field of divergence. When the residual is separated into spatial high and low passes, they obtain similar results to ours, with the low pass being mainly divergent but the high pass having a small-scale structure similar to ∇^2SST.

b. *Forcing of small-scale divergence field*

It was remarked above that Fig. 8e shows structure related to the SST field. This is next quantified by applying a boundary layer model, similar to that of Lindzen and Nigam (1987), Stevens et al. (2002), Back and Bretherton (2009), Takatama et al. (2015), and Duffy et al. (2020). In our approach, we calculate hydrostatic boundary layer pressure perturbations from the boundary layer virtual temperature T_v [Eq. (9) of Duffy et al. 2020], then estimate the surface divergence field using Eq. (12) of the same paper, which is repeated here:

$$\nabla \cdot \underline{\mathbf{U}} \cong \frac{p_s g \varepsilon}{R_d \rho_0 (\varepsilon^2 + f^2)} \int_{\text{surface}}^{H} \frac{\nabla^2 T_v}{T_v^2} dz, \tag{2}$$

where $\underline{\mathbf{U}}$ is the depth-averaged horizontal wind vector, p_s is surface pressure, g is the acceleration due to gravity, R_d is the gas constant for dry air, ρ_0 is a reference air density (we use $\rho_0 = 1.225$), f is the Coriolis acceleration, T_v is the virtual temperature, and H is the height of the boundary layer. Note that for the calculation of hydrostatic boundary layer pressure perturbations and of the estimated surface divergence field, we assume that pressure perturbations above H are zero. This is all done using monthly mean values for December 2018. The key step is to have some knowledge of the planetary boundary layer (PBL) friction coefficient ε (Rayleigh drag; note that we neglect the effects of entrainment at the top of the boundary layer.) Here, ε is estimated from $\epsilon = |\underline{\boldsymbol{\tau}}|/(|\underline{\mathbf{U}}|H)$ [corrected from Takatama et al. (2015)], where $\underline{\boldsymbol{\tau}}$ is the wind stress vector, and $\underline{\boldsymbol{\tau}}$ and $\underline{\mathbf{U}}$ are both monthly means for December 2018.

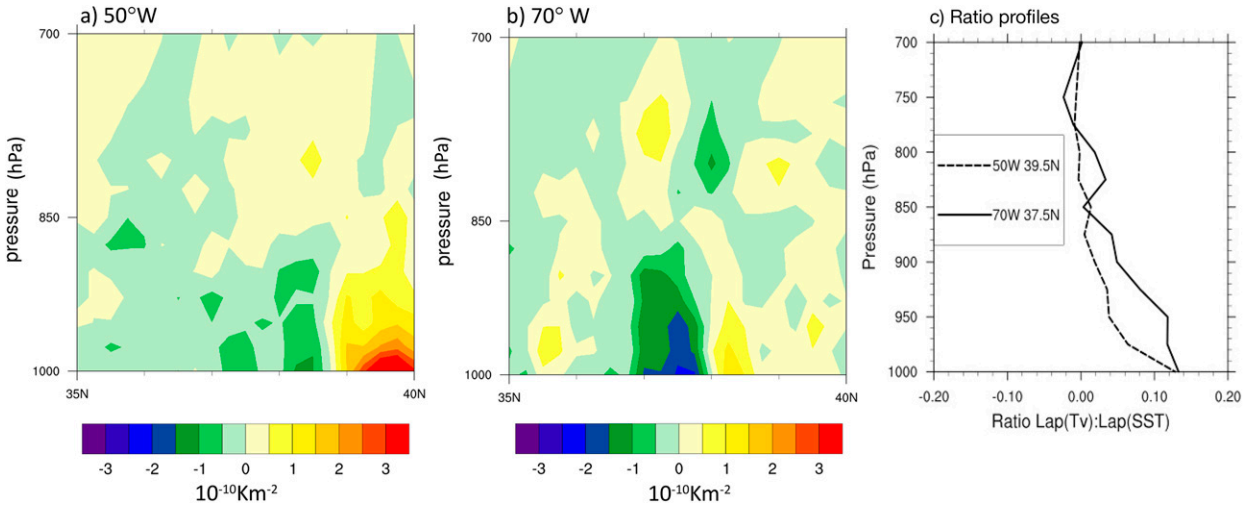

FIG. 9. The variation of Lap(T_v) with pressure from 1000 to 700 hPa. (a) Vertical cross section of Lap(T_v) at (a) 50°W and (b) 70°W. (c) Vertical profiles of the ratio of Lap(T_v) to Lap(SST) through the center of features.

We test two approaches motivated by Back and Bretherton (2009) and Duffy et al. (2020):

- Method 1: Use monthly mean air temperature and humidity from ERA5 to compute T_v. Then, by comparing the estimated divergence field from Eq. (2) with the actual divergence field, we can investigate how well the boundary layer model represents the wind divergence response to realistic pressure gradients.
- Method 2: In the second approach, $\nabla^2 T_v$ is estimated empirically from ∇^2SST, as detailed below. This allows for an estimate of the surface divergence field directly as a function of ∇^2SST. Comparing the estimate with our term 3 of the decomposition should reveal how well the boundary layer model simulates SST-forced effects.

For the second approach, $\nabla^2 T_v$ is estimated from ∇^2SST as follows. First, note that the spatial patterns of $\nabla^2 T_v$ at different heights in the boundary layer look similar to ∇^2SST but are drastically weaker in magnitude (Fig. S7). Vertical sections of $\nabla^2 T_v$ that cut through prominent SST features are next examined. A section at 50°W (Fig. 9a) passes across a cold SST eddy between 39° and 40°N and has positive ∇^2SST and $\nabla^2 T_v$. Another section, at 70°W (Fig. 9b), crosses the Gulf Stream northeast of Cape Hatteras between 37° and 38°N, associated with negative ∇^2SST and $\nabla^2 T_v$. In both cases, $\nabla^2 T_v$ rapidly decays with height, approaching zero at 850 hPa at 50°W (Fig. 9a), while exhibiting a dipole in the vertical at 70°W with a weak oppositely signed pole above 850 hPa (Fig. 9b). The ratio $R = \nabla^2 T_v / \nabla^2 SST$ is shown as a function of height through the center of these features in Fig. 9c. [Note that R is already small, ~0.1, at 1000 hPa and gets smaller above, as can be anticipated from Fig. S7. This decay with height is much more rapid than is assumed for the tropical investigations of, for example, Lindzen and Nigam (1987) and Duffy et al. (2020), and this is likely due to the much smaller scale of the Gulf Stream SST field compared to the tropics.]

We then estimate $\nabla^2 T_v$ throughout the domain using

$$\nabla^2 T_v(x, y, p) \cong R(p) \nabla^2 SST(x, y), \tag{3}$$

where p is pressure, choosing $R(p)$ from one of the profiles in Fig. 9c. In other words, a fixed decay with height of $\nabla^2 T_v$ is applied at every grid point within the domain. For method 2, the vertical integration in Eq. (2) is done to local PBL height. Further, we use lowest-model level T_v for the denominator in the integrand in Eq. (2), but SST could also be used.

The key results from these approaches were as follows:

(i) The first result was that boundary layer–averaged Laplacian of ERA5 virtual temperature T_v ($\nabla^2 T_{v\text{pbl}}$; Fig. 10a, as used in method 1) had many similarities with ∇^2T2m (Fig. 1c) and ∇^2SST (Fig. 1b), indicating that for this monthly mean case, the gradients in the SST field were determining most of the boundary layer horizontal temperature gradient fields. However, the magnitude of $\nabla^2 T_{v\text{pbl}}$ was about an order of magnitude smaller than ∇^2T2m, due to smoothing effects by thermal advection.

(ii) Second, the Laplacian of boundary layer pressure perturbations (from method 1) was virtually identical to ∇^2SLP (Fig. S8), meaning that pressure perturbations above the boundary layer had little effect on ∇^2SLP. Referring back to Eq. (1) of this paper, it implies that the second term on the right-hand side is dominant for this monthly mean case.

(iii) Next, the estimated near-surface divergence Eq. (2) using method 1 was derived assuming the depth of the boundary layer H is equal to the local PBL height (Fig. 10b), and alternative results assuming H is the height of the 850-hPa surface are shown in Fig. S9. The corresponding friction coefficients ε are shown in Fig. S10. The estimated divergence field (Fig. 10b) shares some features with the actual divergence field at 10 m (Fig. 10c) but appears to have a finer-scale structure and is a bit weaker. The magnitude of

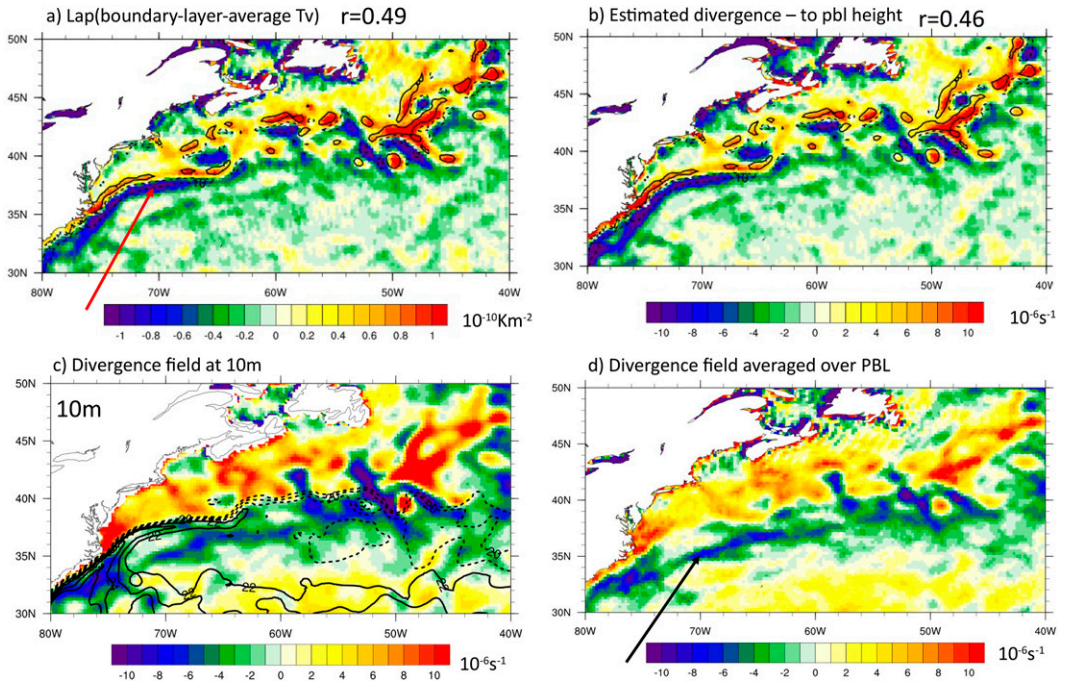

FIG. 10. Comparison of boundary layer modeled divergence field with actual divergence field from ERA5, December 2018 monthly mean. This uses method 1 of section 4b. (a) The Laplacian of boundary layer–averaged virtual air temperature and (b) the estimated divergence field using (2) and integrating to the local PBL height. (c) The ERA5 divergence field at 10 m and (d) the ERA5 divergence field averaged over the local PBL height. Contours in (a) and (b) are Laplacian (SST). Contours in (c) are SST as in Fig. 1. In (a) and (b), the correlation r with 10-m divergence is shown.

features in the estimated divergence field compares better with the divergence field from ERA5 depth averaged to the PBL height (Fig. 10d), which seems reasonable given that Eq. (2) shows the depth-averaged divergence.

(iv) When using method 2 (Figs. 11a,b), the estimated divergence field is somewhat more fine structured than using method 1, as expected since it is mainly a function of ∇^2SST. A slightly stronger divergence field is obtained when using $R(p)$ from 37.5°N, 70°W (Fig. 11b) than from 39.5°N, 50°W, which may be anticipated from Fig. 9c, which shows generally larger values of $R(p)$ at the former location up to 800 hPa. Note that although the results of method 2 do not look very similar to the mean ERA5 divergence averaged over the PBL (Fig. 11c), they do bear a close resemblance to the median high-pass divergence at 10 m (term 3; Fig. 11d), supporting our hypotheses that the latter is mainly influenced by SST–boundary layer processes. However, the pattern correlation s between estimates from method 2 and the median high-pass divergence at 10 m has a lower value ($s = 0.21$) than that between method 1 and mean divergence ($r = 0.46$). This is partly because the assumption that all small-scale features in nonextreme divergence are due to SST is not perfect, and also the use of a fixed vertical profile $R(p)$ excludes the possibility of spatial lags (tilting) of anomalies of $\nabla^2 T_v$ in the vertical.

(v) Both method 1 and method 2 give an estimated band of convergence along the Gulf Stream northeast of Cape Hatteras (e.g., between 75° and 70°W; see red arrow in Fig. 10a) that is too strong and too narrow compared to the actual convergence from ERA5 (Figs. 10 and 11). Meanwhile, a band of convergence located to the south of this in the mean ERA5 field between 70° and 65°W (black arrow in Fig. 10d) is not well estimated. The latter does not appear in the median high-pass divergence field (Fig. 11d), and thus it may be considered an extreme (see also Fig. S13a).

The fact that the boundary layer model applying method 1 (using monthly mean ERA5 $\nabla^2 T_v$ and consequently realistic ∇^2SLP) does not well reproduce this signature of an extreme suggests a limitation of the boundary layer model response to extremes. Conversely, the fact that both method 1 and method 2 show a too-strong convergence along the Gulf Stream (red arrow, Fig. 10a) suggests a further limitation of the boundary layer model in its response to SST. Limitations may include the absence of entrainment and vertical mixing in our implementation, the oversimplicity of linearized Raleigh drag, inaccurate friction coefficients, and the absence of nonlinear and tendency momentum budget terms in the boundary layer model formulation. For example, the vertical-mixing effect may modify the effect of $\nabla^2 T_{v\text{pbl}}$, as suggested by the downwind SST gradient that often takes positive values (Fig. 1e), which would favor surface divergence and, possibly,

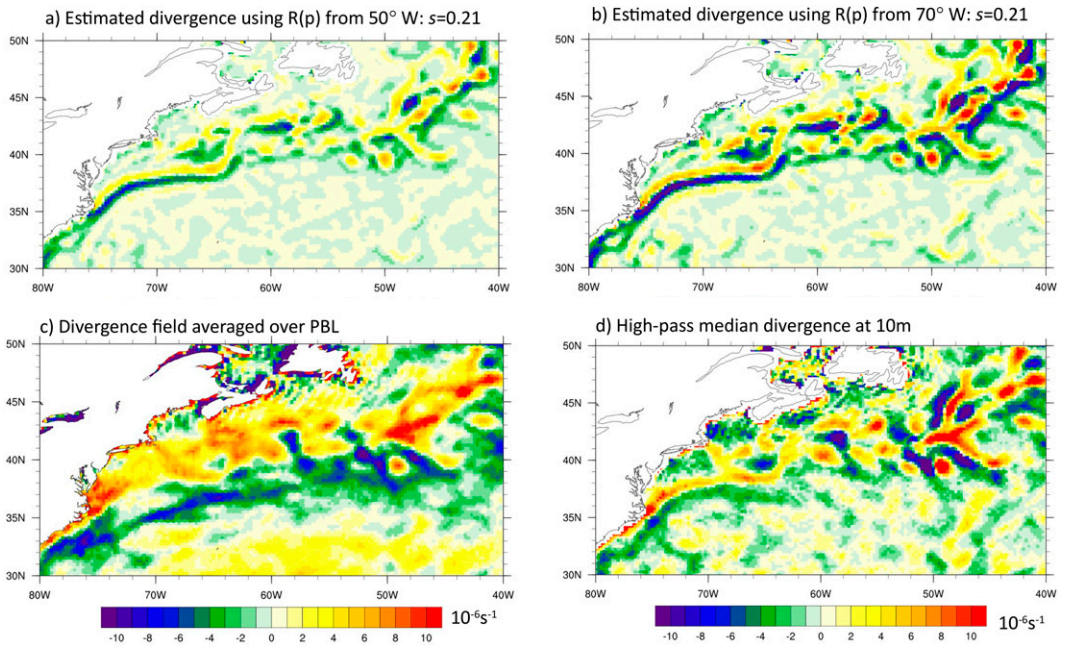

FIG. 11. Estimates of the divergence field following method 2 of section 4b for December 2018. (a) Using $R(p)$ from 39.5°N, 50°W and (b) using $R(p)$ from 37.5°N, 70°W. (c) The ERA5 mean divergence field averaged over the local PBL height, as in Figs. 10d, and (d) the ERA5 high-pass median divergence field at 10 m, a close-up of Fig. 8e. In (a) and (b), the correlation s with high-pass median divergence is shown. All panels share the same color bar.

a relative weakening of the overstrong convergence band along the Gulf Stream in the estimate.

It should also be noted that as the vertical motion at the top of the boundary layer is related to the vertical integral of the divergence via continuity (see also section 5), our boundary layer model estimates imply vertical motion directly over the Gulf Stream that is too strong and vertical motion resulting from the extreme event that is too weak.

The companion paper (N. Schneider et al. 2023, unpublished manuscript) addresses some of these limitations using a more sophisticated boundary layer model and an analysis approach that fully takes into account background wind direction and high-frequency variability. The remaining focus of this paper instead is on the implications of the near-surface convergence for processes higher in the boundary layer and in the free troposphere, as seen in the ERA5 system with full dynamics and assimilation.

5. Vertical structure and precipitation

a. *Vertical structure of time-mean fields*

Inspection of monthly average divergence fields at various heights (Fig. 12) reveals that the overall magnitude of the divergence and convergence signals reduces with height from a maximum near the surface (Fig. 12a), and also that the mesoscale signatures (e.g., in red box) decay fairly rapidly with height (e.g., by 900 hPa; Fig. 12b). The main band of convergence shifts to the north and west by 700 hPa (Fig. 12c), while in the upper troposphere, there is mostly divergence above the Gulf Stream (Fig. 12d), but not as clearly defined as in the longer-term average shown in Minobe et al. (2008).

In contrast, the vertical motion, as represented by the time derivative of pressure (referred to as omega), strengthens with height (Fig. 13), with the largest magnitudes between 850 and 700 hPa (Figs. 13b,c), with some weakening and less coherent structure at higher levels (Fig. 13d). The mesoscale signatures (red box) remain strong until at least 850 hPa (Fig. 13b), but again weaken at higher levels (Figs. 13c,d). The strengthening of the vertical velocity structure with height to 850 hPa, for example, for mesoscale signatures, is to be expected from continuity, where the strong convergence in the lowest layers of the atmosphere is accumulated in a vertical integral to form the upward motion.

b. *Precipitation*

In this subsection, we ask how the results on NSWC discussed above relate to precipitation. Note that different results may apply as to whether the precipitation is stratiform or convective. Stratiform precipitation results from widespread updrafts such as those found at midlatitude fronts, or at surface lows, whereas convective precipitation results from buoyant ascent that tends to be orders of magnitude larger than the ascent driving stratiform precipitation. It is noted, however, that convective rainfall frequently occurs in the vicinity of stratiform precipitation as the associated widespread ascent reduces the atmospheric stability. As such, there is a strong relationship between NSWC and precipitation. Stratiform precipitation is also known as large-scale or resolved precipitation in models, while convective precipitation is typically

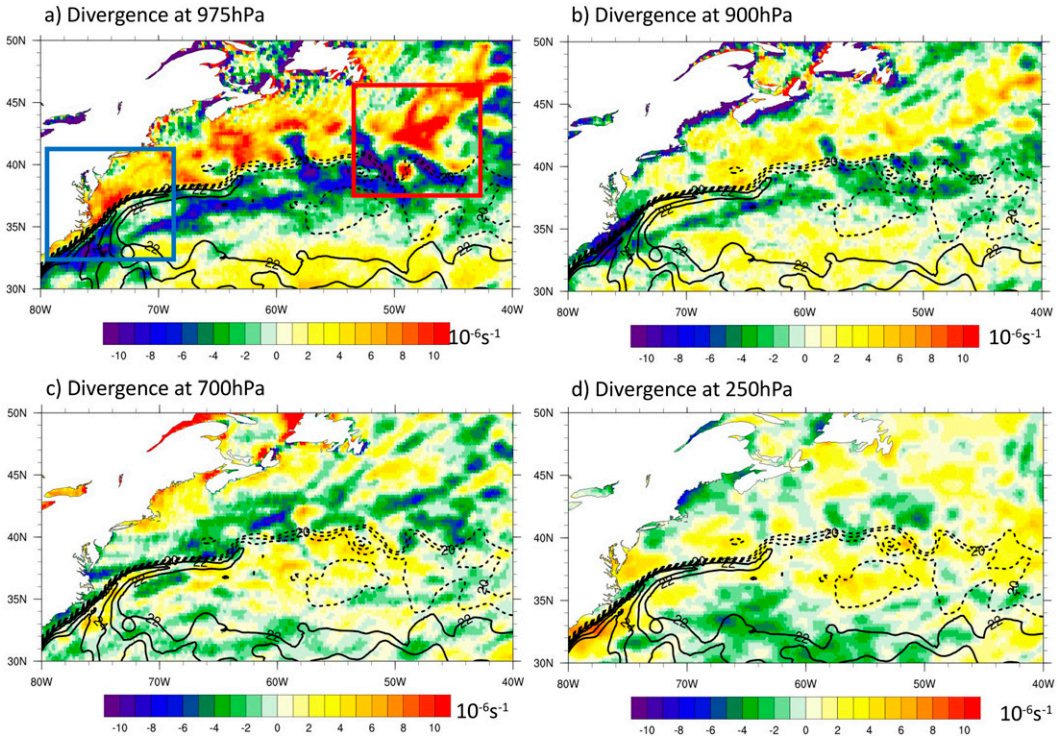

FIG. 12. Divergence field at different vertical levels, one-month average, December 2018. As in Fig. 1, but showing wind divergence at various vertical levels, as indicated. Note that the mesoscale signatures (e.g., in red box) decay fairly rapidly with height. SST contours are overlaid as in Fig. 1.

subgrid scale (except for very high-resolution models) and is parameterized, including in ERA5 (see section 2a).

This is illustrated with examples of hourly accumulations (converted to mm day^{-1}) of both stratiform and convective precipitation in Figs. 14a and 14c, for a time stamp close to that of Fig. 2. As expected, the precipitation field is noticeably dominated by the two atmospheric frontal systems (one in the central to western basin, the other centered over the United Kingdom), with the stratiform (large scale) precipitation exhibiting a larger magnitude than the convective precipitation. The total precipitation field (Fig. 14b) aligns well with the instantaneous NSWC extremes (Fig. 14d).

The monthly averaged case is examined next. It is already well known that in the midlatitude storm tracks, atmospheric fronts are responsible for up to 90% of the rainfall (Catto et al. 2014), although this result depends on the resolution of the dataset analyzed (Soster and Parfitt 2022). Is there also evidence of the precipitation being organized by the boundary layer processes discussed in sections 4a and 4b?

For the December 2018 monthly mean case, the large-scale or stratiform precipitation is widespread in the northwest Atlantic (Figs. 15a,c), and there is a hint of a spatial relationship with the mean minus median divergence field metric including the clustering near the Gulf Stream (cf. with Fig. 8a). Meanwhile, the convective precipitation in this month (Figs. 15b,d) resembles aspects of the 850-hPa vertical motion (Fig. 13b) and near-surface wind divergence fields (Figs. 1f and 8f), with minimal precipitation inshore of the Gulf Stream, where there is surface divergence and downward motion on average, and maxima in precipitation where the NSWC and upward motion is strong over the Gulf Stream, including evidence of mesoscale ocean structure. As discussed above (sections 4 and 5a), the near-surface wind divergence and 850-hPa upward motion are, in turn, partly controlled by the boundary layer response to ∇^2SST and the downwind SST gradient. (To emphasize the fact that the convective precipitation is strongly controlled by the SST, SST contours are overlaid on Fig. 15d, showing that the ocean front separates the strong convective precipitation on the warm side from weaker precipitation on the cold side.) Similar results are found for December 2016 mean precipitation (Fig. S11).

Overall, the picture emerges that even if the mean field is mainly an accumulation of precipitation in passing atmospheric fronts, which, at first sight, do not seem to have an obvious relationship to the SST field (Fig. 2), the warm side of the Gulf Stream and North Atlantic Current stand out as dominant regions for enhanced precipitation. This leads to the question of whether the fronts are being generated by the Gulf Stream system via the influence on the boundary layer, or if they are simply having their moisture content modified by the warm water, or a combination of the two. This and related questions are discussed in section 6c.

A more quantitative assessment of the relationship between precipitation and the near-surface divergence field can be gleaned from spectral analysis, in a similar approach to section 3b. The two fields are mostly out of phase, as expected,

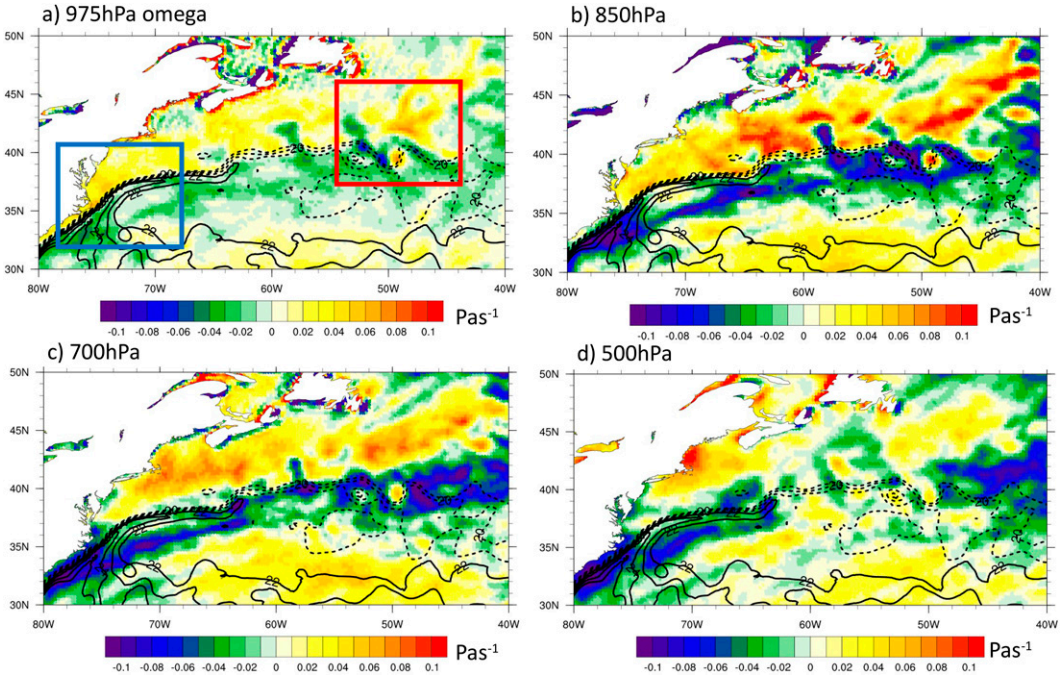

FIG. 13. Vertical pressure velocity omega at various vertical levels, as indicated, for a one-month average, December 2018. Negative values are upward velocities. The mesoscale signatures [e.g., red box in (a)] remain strong until at least 850 hPa but weaken at higher levels.

particularly for the low-wavenumber regime where coherence is high (Figs. 16c,h). The resolved, stratiform precipitation has very weak coherence (with the divergence field) at all wavelengths less than about 1000 km (Fig. 16a), whereas the convective precipitation has a secondary peak in the mesoscale regime already identified previously (see Figs. 6 and 7) that is circled in Fig. 16b. In this regime, the phase difference is between 90° and 180° (Fig. 16f). The narrow region of influence of the boundary layer pressure-adjustment mechanism is confirmed by cross-spectral statistics between precipitation and ∇^2SST, which indicate a response only in the mesoscale (circled) region and only in convective precipitation (Fig. S12).

6. Discussion

a. *How does this relate to previous work?*

This paper aims to reconcile previous work, using a state-of-the-art reanalysis, and it has highlighted a combination of processes that give rise to the NSWC. These processes were identified in previous work, but their relative role was debated. For example, Feliks et al. (2004, 2007) diagnose a boundary layer–forced response plus an upper-level response; see also Brachet et al. (2012). Their decomposition [Eq. (1) here] provides insight into the processes at work and inspires the decomposition in section 4a. Those authors did not explicitly discuss atmospheric fronts, although Brachet et al. (2012) did discuss the role of synoptic variability. They also identified a 10-day time scale as dividing out the synoptic compared with longer-term processes, similar to the present results.

Meanwhile, Minobe et al. (2008) discussed both the role of the boundary layer–forced NSWC and synoptic storm processes but did not fully separate their contributions. However, they noted the similarity of the divergence field to ∇^2SST, which we show is not just coincidence—∇^2(SST and T2m) are indeed important forcing factors at particular time and space scales. Minobe et al. (2010) and Kuwano-Yoshida et al. (2010) also show that the vast majority of the precipitation response to the SST front relaxation is from convective precipitation, not stratiform precipitation. Following on from that work, Takatama et al. (2015) investigated the strong relationship of the divergence field to ∇^2SLP and quoted this as evidence of the pressure-adjustment mechanism, but they did not quantify the key link between ∇^2SLP and ∇^2SST, which is not active on all time scales (see Figs. 2 and 7).

O'Neill et al. (2017) illustrated the strong influence of extremes on the time-mean divergence field, but, as mentioned above, they also show the importance of the large-scale divergence, as well as results hinting at the presence of small-scale boundary layer processes (section 4a).

Parfitt and Seo (2018) identified the importance of atmosphere fronts, suggesting they contribute almost all of the time-mean NSWC over the Gulf Stream, using conditional analysis. Their findings were based on the divergence field at 900 hPa. Our Fig. 12 shows that the signature of the mesoscale ocean on divergence is much weaker at 900 hPa than at the surface;–however, the important vertical motion field strengthens up to at least 850 hPa. Our Fig. 8 also shows that when the extremes are removed, the overall field is mostly divergent, consistent with Parfitt and Seo (2018), and

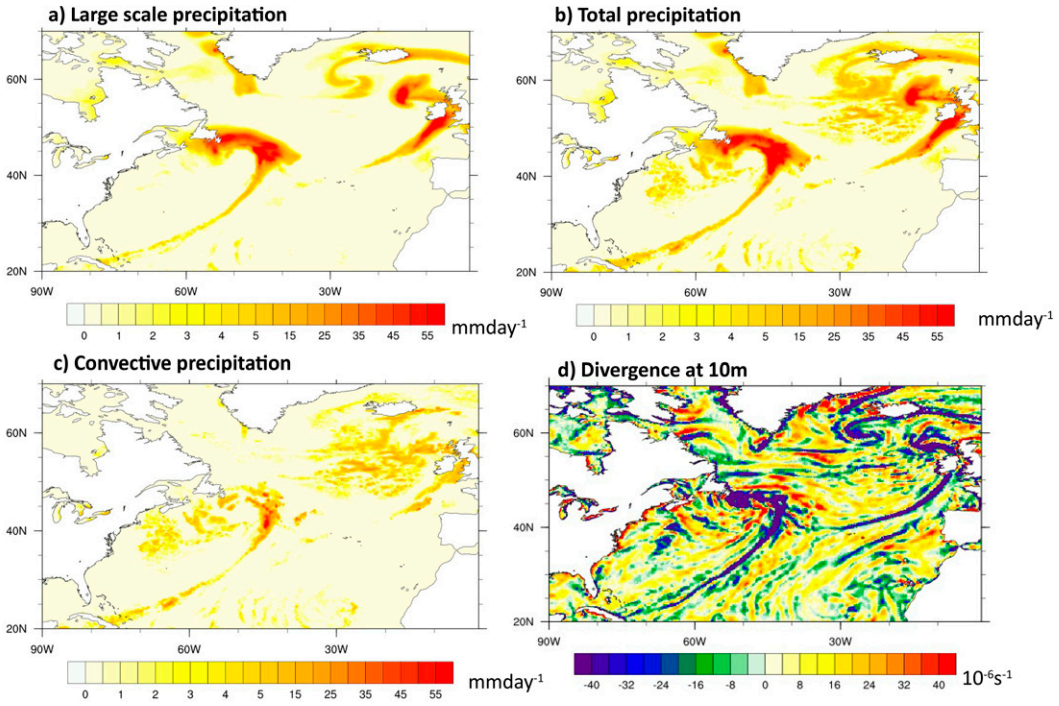

FIG. 14. Precipitation fields in December 2018: precipitation at time stamp corresponding to Fig. 2. (a) Large-scale, stratiform part, (b) total, and (c) convective part. The corresponding near-surface divergence field is shown in (d), repeated from Fig. 2. Note the nonlinear color scale for precipitation, every 0.5 mm day^{-1} to 5 mm day^{-1}, then every 5 mm day^{-1} thereafter.

it is only when a spatial filter is applied to this residual field that the boundary layer impact is visible.

b. *Dynamics of processes forcing divergence field variability*

This paper has not aimed to make a full investigation of the dynamics and thermodynamics occurring either in the atmosphere frontal processes, or the SST-driven boundary layer response, excepting the brief diagnosis in section 4b. Full investigations have been done elsewhere (e.g., see recent papers Wenegrat and Arthur 2018; Skyllingstad et al. 2019; Sullivan et al. 2020, 2021; Sullivan and McWilliams 2022; Schneider 2020; Reeder et al. 2021; Masunaga and Schneider 2022; N. Schneider et al. 2023, unpublished manuscript). However, the analysis presented here, in particular the spectral coherence results, hints at dynamics such as the following:

(i) From existing literature and theory, the expectation is that under low wind speeds, the pressure-adjustment mechanism (represented by ∇^2SST and ∇^2SLP) is most important for boundary layer convergence, but at higher wind speeds, the vertical mixing dominates (represented by the downwind SST gradient) (Spall 2007; Schneider and Qiu 2015; Schneider 2020; Samelson et al. 2020). The Gulf Stream region in winter often experiences strong winds (see, e.g., Marshall et al. 2009), which may hint of a bigger effect of vertical mixing, for which a metric is the downwind SST gradient. However, section 4b points at a role also for the pressure-adjustment mechanism, and both processes are likely important. Takatama et al. (2015) suggest that vertical mixing is most important for the wind curl, while pressure adjustment mainly drives the small-scale divergence field on time scales of a month and more.

(ii) The results of this paper could be interpreted as particular processes only acting at certain time and space scales (suggested, e.g., by the spectral analysis of section 3b) Another, subtly different, interpretation is that the processes dominate at certain scales but still operate at other scales, albeit with a weak magnitude that may not rise above the noise level. The spectral analysis could then be reinterpreted as, for example, synoptic storms and atmospheric fronts dominating at subdaily time scales, with such regularity and large magnitude that the boundary layer response is not distinguishable from noise. Further, it should be noted that SST fields (on the reanalysis grid of ~0.31°) do not change much on shorter-than-10-day time scales, so that methods such as coherence and regressions will struggle to detect any response to SST at these time scales.

(iii) A companion paper by (N. Schneider et al. 2023, unpublished manuscript) explores the previous point further, based on the approximation that the divergence field is the sum of 1) synoptic/frontal variations, 2) boundary layer variations driven directly by the underlying SST, and 3) their interactions. The additional consideration

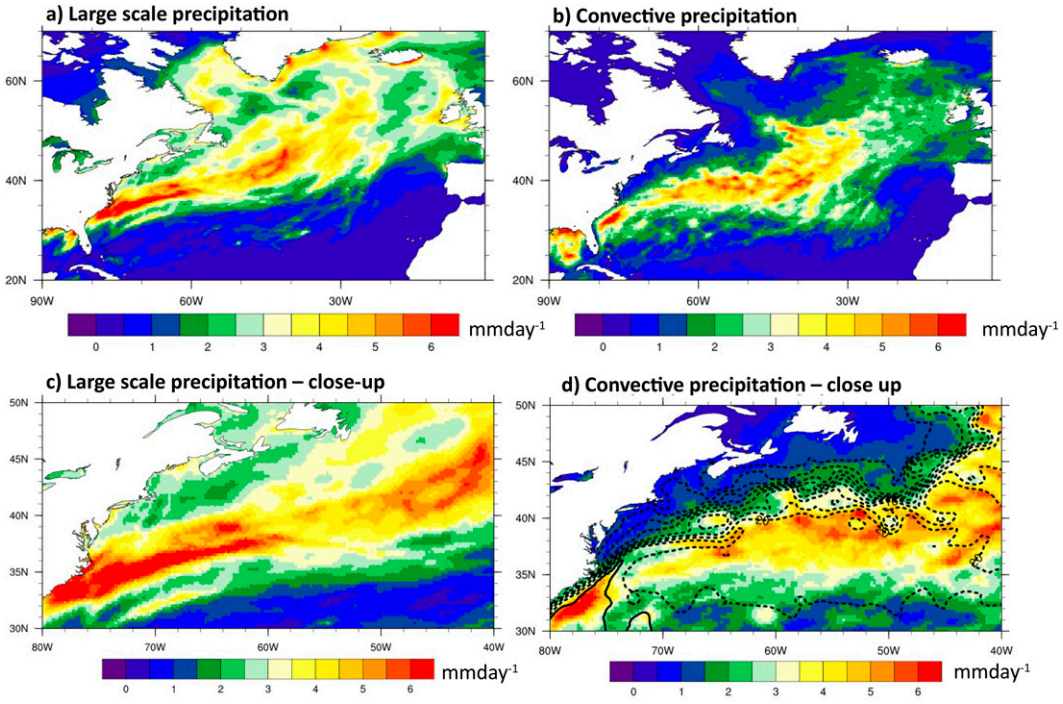

FIG. 15. Monthly average precipitation fields from December 2018. (a),(c) Large-scale (stratiform) precipitation and (b),(d) convective precipitation. The lower panels are respective close-ups of the Gulf Stream region. SST contours are overlaid in (d).

to that detailed in the current paper is that the direct SST influence (2) is itself modified by the synoptic variations in wind. (We briefly touch on it here by considering the downwind SST gradient in sections 3a and 4b.) The more comprehensive approach of N. Schneider et al. (2023, unpublished manuscript) allows for clean separation of, for example, pressure gradient and vertical-mixing effects, but is limited by not explicitly including the effect of underlying SST on atmosphere fronts and storms via the boundary layer.

(iv) Another approach to separate out the role of intrinsic atmosphere dynamics from the boundary layer process is to use ensemble averages of atmosphere state. An example is the high-resolution "interactive ensemble" of Kirtman et al. (2017), where the average of an ensemble of atmosphere simulations is used to force a single ocean model (and the ocean state in turn is passed to each of the atmosphere ensemble members). A main result from their work was that the correlation between monthly anomalies of SST and convective precipitation is much higher when using the ensemble average, which has much of the atmosphere weather "noise" removed, than for a given ensemble member, or for a regular high-resolution coupled model. Particularly large correlations are seen in western boundary currents like the Gulf Stream. As convective precipitation and NSWC are dynamically related (e.g., see Figs. 14–16), it is likely that a similar result would hold for NSWC in the interactive ensemble. Future work could explore the interactive ensemble as an approach to distinguish the different processes at work, especially at short time scales where normally the synoptic variability dominates.

c. *On the influence of boundary layer process on extreme events*

In this paper, boundary layer processes and extreme events have been treated, for the most part, as independent. However, there should be some interaction, as alluded to in point (iii) of the previous subsection. Here, we expand on this.

First, from a storm-track perspective, Nakamura et al. (2004), Hotta and Nakamura (2011), Small et al. (2014), Kuwano-Yoshida and Minobe (2017) and many others have noted that low-level atmosphere temperature gradients (in the horizontal and vertical) are affected by SST fronts such as the Gulf Stream, via diabatic heating from the surface, in turn modifying and often strengthening the atmospheric baroclinicity that synoptic eddies feed off. The atmosphere fronts associated with synoptic eddies are the likely cause of most extreme events over the Gulf Stream, especially in winter, as identified by, for example, O'Neill et al. (2017) and Parfitt and Seo (2018).

Reeder et al. (2021) examined this further and classified frontogenesis in the region, subdividing it into adiabatic frontogenesis (fronts formed due to dynamic mechanisms) and diabatic frontogenesis (fronts formed due to thermodynamic mechanisms such as differential surface heating). They concluded that diabatic frontogenesis could occur over the Gulf Stream but only when strong preexisting fronts were not

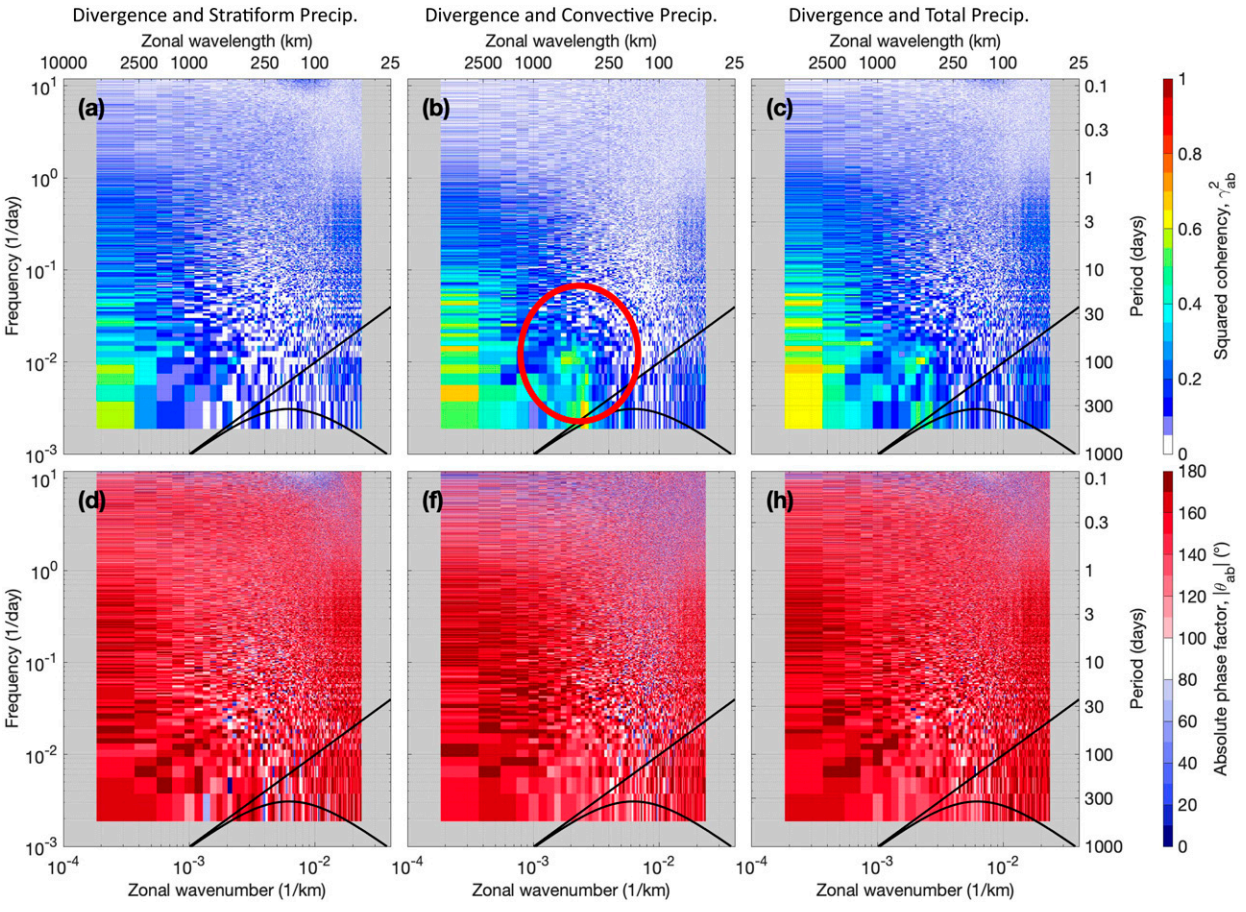

FIG. 16. Wavenumber–frequency spectra between near-surface divergence and precipitation. As in Fig. 6, but for (a),(d) large-scale (stratiform) precipitation; (b),(f) convective parameterization; and (c),(h) total precipitation.

present in the airflow. (An implication of this is that the kind of situation shown in Fig. 2 of this paper is not ideal for frontogenesis over the Gulf Stream.)

Masunaga et al. (2020a,b) suggest some link between the occurrence of atmosphere fronts and boundary layer processes. They showed that typical weather patterns ("clusters") associated with NSWC over the Gulf Stream in the JRA-55 reanalysis (Kobayashi et al. 2015) were associated with frontal occurrence suggested to be due to diabatic heating from the surface.

Diabatic frontogenesis over the Gulf Stream is due to large sensible heat flux gradients (Parfitt et al. 2016; Parfitt and Kwon 2020), which are also essential to the pressure gradient mechanism (and may occur concurrently with vertical mixing). Further, the adiabatic term also has a temperature gradient dependence, and as such, any diabatic effects as communicated through the pressure-adjustment mechanism can still potentially influence the extreme fronts that are adiabatically dominated. Thus, we see a link between the boundary layer mechanisms and the extreme events.

The possibility that the processes discussed by Minobe et al. (2008) may occur in individual storms has also been investigated by Vannière et al. (2017a), identifying the pressure-adjustment mechanism working in the cold sector of a storm, once again due to the large sensible and latent heat fluxes.

The key question is how dominant are the processes identified above? Reeder et al. (2021) found a bigger influence of adiabatic frontogenesis than diabatic frontogenesis when preexisting fronts were in the airflow. Further, cold-sector precipitation found by Vannière et al. (2017b) was about 13% of the total precipitation in a long record from ERA-Interim.

Further insight can be gained from Fig. 8a, the map of extremes in the month of December 2018. A close inspection reveals one particularly strong feature (arrowed in the figure), which lies almost along the Gulf Stream front. This could be an example of strong "diabatic frontogenesis" (due to one event, or to a series of instantaneous events occurring at the same location), whereas most of the rest of the field in Fig. 8a is from adiabatic frontogenesis (more simply, the strong propagating storms like those in Fig. 2). A close-up of Fig. 8a, with SST contours overlaid, is shown in Fig. S13, together with a similar example from another year. The mechanisms for extremes such as these will be a subject of future work.

7. Conclusions

This paper has reinvestigated NSWC over the Gulf Stream and its relationship to SST, vertical motion, and precipitation. It finds that the various processes identified in previous work are all operating but are dominant at different space and time scales. In general, previous work used isolated metrics or theories that tended to highlight one mechanism over another; in contrast, our work is able to separate out and quantify the different processes. The high-resolution ERA5 reanalysis data are used for the current investigation. ERA5 has a reasonable representation of extremes and small-scale structures, although previous work has shown it underestimates wind response to SST by 20%–30%.

Specifically, NSWC at short time scales of 10 days or less shows the prominent signature of the frontal components of atmospheric weather systems, but on longer time scales, the influence of boundary layer processes directly relating to the underlying SST becomes more visible as atmosphere fronts are averaged out to some extent, although they do leave an important residual. Both these processes occur over similar spatial scales (atmosphere fronts are ~100 km across front but can extend thousands of kilometers along front; the Gulf Stream has a similar extent and width) and so applying spatial filters to isolate the features can be challenging. In this paper, a simple approach has been used to isolate extreme events (which are usually attributed to atmosphere fronts) via differencing the mean and median fields.

It is found that the time-mean divergence field comprises three main parts:

1) Atmosphere fronts and extremes mainly acting on synoptic time scales but leaving a residual of convergence in the time mean.
2) A background, large-scale divergence.
3) A small-scale structure impacted by SST and boundary layer processes.

In fact, these processes can be interlinked; for example, direct boundary layer responses to SST could induce quasistationary fronts (Masunaga et al. 2020a,b), combining parts 1 and 3.

Quantitatively, all these contributions have local amplitudes up to $1 \times 10^{-5}\ s^{-1}$, comparable to the time-average total field (see Fig. 8). Note that as parts 1 and 2 above have mostly one sign over the region of interest, whereas part 3 is dual signed with no dominant sign, it can be inferred that parts 1 and 2 make a larger contribution when averaged over a large spatial area.

A boundary layer model is used to interpret the findings above. This idealized model showed some skill in reproducing the ERA5 near-surface divergence field, except that it overestimated the convergence occurring over the Gulf Stream after it separates from the coast at Cape Hatteras, while it underestimated the effect of extremes on the divergence field.

As well as NSWC, the vertical structure of convergence and of vertical motion was investigated, and it was found that the small-scale SST-forced signature in the divergence field rapidly decayed with height within the boundary layer, whereas the signature in vertical motion extended to ~850–700 hPa. The resulting precipitation fields hinted at directly SST-forced structure in the convective part, whereas the large-scale (stratiform) part showed a broader spread of precipitation likely associated with clustering of atmospheric fronts around the Gulf Stream/western basin.

Recent work has identified remote response to the Gulf Stream mean state and variability (Hand et al. 2014; Wills et al. 2016; Siqueira and Kirtman 2016; Lee et al. 2018). The precipitation results just discussed suggest that some of the remote response is due to direct response to SST variability (via convective part and subsequent diabatic heating) and some is due to modulation of atmosphere front clustering (stratiform part). To quantify the impact of these two paths on remote response would be useful future work, as would be an assessment of the ERA5 precipitation relative to satellite data and other reanalyses.

Acknowledgments. This paper was greatly improved following the suggestions from three anonymous reviewers who are thanked. The work was partly produced by VR during a collaborative visit from CERFACS to NCAR in 2019. Bob Tomas is thanked for contributing to early versions of this work. Discussions with Hisashi Nakamura, Shoshiro Minobe, Larissa Back, Margaret Duffy, and Arnaud Czaja were much appreciated. Laurent Terray recommended use of the state-of-the-art ERA5 dataset and also pointed the authors to Eq. (1) taken from Brachet et al. (2012). RJS, RP, NS, and LL were partly funded by NOAA CVP Grants NA22OAR4310615, NA22OAR4310616, and NA22OAR4310617. RJS was funded in part by the International Laboratory for High Resolution Earth System Prediction, a collaboration between QNML, China, Texas A&M, and NCAR. Computing and data storage resources, including the Cheyenne supercomputer (https://doi.org/10.5065/D6RX99HX), were provided by the Computational and Information Systems Laboratory (CISL) at NCAR. This material is based upon work supported by the National Center for Atmospheric Research, which is a major facility sponsored by the NSF under Cooperative Agreement 1852977. NS was supported by National Aeronautics and Space Administration Grant 80NSSC19K0058 and by the JAMSTEC IPRC Collaborative Research (JICoRe). LO was partly funded by NASA Grant 80NSSC19K1117.

Data availability statement. ERA5 data were gathered from the NCAR Research Data Archive (RDA), https://rda.ucar.edu/datasets/ds633.0/ and https://rda.ucar.edu/datasets/ds633.1/, where the data are on a 0.25° latitude–longitude grid and accessed between October 2019 and December 2022. CCMP v03.0 data were gathered from Remote Sensing Systems (https://www.remss.com/measurements/ccmp/) at the following data location on 14 November 2022: https://data.remss.com/ccmp/v03.0/monthly/y2018/m12/.

REFERENCES

Atlas, R., R. N. Hoffman, J. Ardizzone, S. M. Leidner, J. C. Jusem, D. K. Smith, and D. Gombos, 2011: A cross-calibrated,

multiplatform ocean surface wind velocity product for meteorological and oceanographic applications. *Bull. Amer. Meteor. Soc.*, **92**, 157–174, https://doi.org/10.1175/2010BAMS2946.1.

Back, L. E., and C. S. Bretherton, 2009: On the relationship between SST gradients, boundary layer winds, and convergence over the tropical oceans. *J. Climate*, **22**, 4182–4196, https://doi.org/10.1175/2009JCLI2392.1.

Bendat, J. S., and A. G. Piersol, 1986: *Random Data: Analysis and Measurement Procedures*. 3rd ed. John Wiley and Sons, 594 pp.

Booth, J. F., L. A. Thompson, J. Patoux, K. A. Kelly, and S. Dickinson, 2010: The signature of midlatitude tropospheric storm tracks in the surface winds. *J. Climate*, **23**, 1160–1174, https://doi.org/10.1175/2009JCLI3064.1.

Brachet, S., F. Codron, Y. Feliks, M. Ghil, H. Le Treut, and E. Simonnet, 2012: Atmospheric circulations induced by a midlatitude SST front: A GCM study. *J. Climate*, **25**, 1847–1853, https://doi.org/10.1175/JCLI-D-11-00329.1.

Catto, J. L., N. Nicholls, C. Jakob, and K. L. Shelton, 2014: Atmospheric fronts in present and future climates. *Geophys. Res. Lett.*, **41**, 7642–7650, https://doi.org/10.1002/2014GL061943.

Chelton, D. B., and Coauthors, 2001: Observations of coupling between surface wind stress and sea surface temperature in the eastern tropical Pacific. *J. Climate*, **14**, 1479–1498, https://doi.org/10.1175/1520-0442(2001)014<1479:OOCBSW>2.0.CO;2.

——, M. G. Schlax, M. H. Freilich, and R. F. Milliff, 2004: Satellite measurements reveal persistent small-scale features in ocean winds. *Science*, **303**, 978–983, https://doi.org/10.1126/science.1091901.

Czaja, A., C. Frankignoul, S. Minobe, and B. Vannière, 2019: Simulating the midlatitude atmospheric circulation: What might we gain from high-resolution modeling of air-sea interactions? *Curr. Climate Change Rep.*, **5**, 390–406, https://doi.org/10.1007/s40641-019-00148-5.

de Szoeke, S. P., and E. D. Maloney, 2020: Atmospheric mixed layer convergence from observed MJO sea surface temperature anomalies. *J. Climate*, **33**, 547–558, https://doi.org/10.1175/JCLI-D-19-0351.1.

Donlon, C., and Coauthors, 2007: The Global Ocean Data Assimilation Experiment High-Resolution Sea Surface Temperature Pilot Project. *Bull. Amer. Meteor. Soc.*, **88**, 1197–1214, https://doi.org/10.1175/BAMS-88-8-1197.

Duffy, M. L., P. A. O'Gorman, and L. E. Back, 2020: Importance of Laplacian of low-level warming for the response of precipitation to climate change over tropical oceans. *J. Climate*, **33**, 4403–4417, https://doi.org/10.1175/JCLI-D-19-0365.1.

Feliks, Y., M. Ghil, and E. Simonnet, 2004: Low-frequency variability in the midlatitude atmosphere induced by an oceanic thermal front. *J. Atmos. Sci.*, **61**, 961–981, https://doi.org/10.1175/1520-0469(2004)061<0961:LVITMA>2.0.CO;2.

——, ——, and ——, 2007: Low-frequency variations in the midlatitude baroclinic atmosphere induced by an oceanic thermal front. *J. Atmos. Sci.*, **64**, 97–116, https://doi.org/10.1175/JAS3780.1.

Foussard, A., G. Lapeyre, and R. Plougonven, 2019: Response of surface wind divergence to mesoscale SST anomalies under different wind conditions. *J. Atmos. Sci.*, **76**, 2065–2082, https://doi.org/10.1175/JAS-D-18-0204.1.

Gill, A. E., 1980: Some simple solutions for heat-induced tropical circulation. *Quart. J. Roy. Meteor. Soc.*, **106**, 447–462, https://doi.org/10.1002/qj.49710644905.

Hand, R., N. Keenlyside, N.-E. Omarani, and M. Latif, 2014: Simulated response to inter-annual SST variations in the Gulf Stream region. *Climate Dyn.*, **42**, 715–731, https://doi.org/10.1007/s00382-013-1715-y.

Hayes, S. P., M. J. McPhaden, and J. M. Wallace, 1989: The influence of sea surface temperature on surface wind in the eastern equatorial Pacific: Weekly to monthly variability. *J. Climate*, **2**, 1500–1506, https://doi.org/10.1175/1520-0442(1989)002<1500:TIOSST>2.0.CO;2.

Hersbach, H., and Coauthors, 2020: The ERA5 global reanalysis. *Quart. J. Roy. Meteor. Soc.*, **146**, 1999–2049, https://doi.org/10.1002/qj.3803.

Hewson, T. D., 1998: Objective fronts. *Meteor. Appl.*, **5**, 37–65, https://doi.org/10.1017/S1350482798000553.

Hoskins, B. J., and K. I. Hodges, 2002: New perspectives on the Northern Hemisphere winter storm tracks. *J. Atmos. Sci.*, **59**, 1041–1061, https://doi.org/10.1175/1520-0469(2002)059<1041:NPOTNH>2.0.CO;2.

Hotta, D., and H. Nakamura, 2011: On the significance of sensible heat supply from the ocean in the maintenance of mean baroclinicity along storm tracks. *J. Climate*, **24**, 3377–3401, https://doi.org/10.1175/2010JCLI3910.1.

Joyce, T. M., Y.-O. Kwon, and L. Yu, 2009: On the relationship between synoptic wintertime atmospheric variability and path shifts in the Gulf Stream and the Kuroshio Extension. *J. Climate*, **22**, 3177–3192, https://doi.org/10.1175/2008JCLI2690.1.

Kirtman, B. P., N. Perlin, and L. Siqueira, 2017: Ocean eddies and climate predictability. *Chaos*, **27**, 126902, https://doi.org/10.1063/1.4990034.

Kobayashi, S., and Coauthors, 2015: The JRA-55 reanalysis: General specifications and basic characteristics. *J. Meteor. Soc. Japan*, **93**, 5–48, https://doi.org/10.2151/jmsj.2015-001.

Kushnir, Y., W. A. Robinson, I. Bladé, N. M. J. Hall, S. Peng, and R. Sutton, 2002: Atmospheric GCM response to extratropical SST anomalies: Synthesis and evaluation. *J. Climate*, **15**, 2233–2256, https://doi.org/10.1175/1520-0442(2002)015<2233:AGRTES>2.0.CO;2.

Kuwano-Yoshida, A., and S. Minobe, 2017: Storm track response to SST fronts in the northwestern Pacific region in an AGCM. *J. Climate*, **30**, 1081–1102, https://doi.org/10.1175/JCLI-D-16-0331.1.

——, ——, and S.-P. Xie, 2010: Precipitation response to the Gulf Stream in an atmospheric GCM. *J. Climate*, **23**, 3676–3698, https://doi.org/10.1175/2010JCLI3261.1.

Lee, R. W., T. J. Woollings, B. J. Hoskins, K. D. Williams, C. H. O'Reilly, and G. Masato, 2018: Impact of Gulf Stream SST biases on the global atmospheric circulation. *Climate Dyn.*, **51**, 3369–3387, https://doi.org/10.1007/s00382-018-4083-9.

Lindzen, R. S., and S. Nigam, 1987: On the role of sea surface temperature gradients in forcing low-level winds and convergence in the tropics. *J. Atmos. Sci.*, **44**, 2418–2436, https://doi.org/10.1175/1520-0469(1987)044<2418:OTROSS>2.0.CO;2.

Maloney, E. D., 2009: The moist static energy budget of a composite tropical intraseasonal oscillation in a climate model. *J. Climate*, **22**, 711–729, https://doi.org/10.1175/2008JCLI2542.1.

Marshall, J., and Coauthors, 2009: The CLIMODE field campaign: Observing the cycle of convection and restratification over the Gulf Stream. *Bull. Amer. Meteor. Soc.*, **90**, 1337–1350, https://doi.org/10.1175/2009BAMS2706.1.

Masunaga, R., and N. Schneider, 2022: Surface wind responses to mesoscale sea surface temperature over western boundary current regions assessed by spectral transfer functions. *J. Atmos. Sci.*, **79**, 1549–1573, https://doi.org/10.1175/JAS-D-21-0125.1.

——, H. Nakamura, B. Taguchi, and T. Miyasaka, 2020a: Processes shaping the frontal-scale time-mean surface wind convergence patterns around the Kuroshio Extension in winter. *J. Climate*, **33**, 3–25, https://doi.org/10.1175/JCLI-D-19-0097.1.

——, ——, ——, and ——, 2020b: Processes shaping the frontal-scale time-mean surface wind convergence patterns around the Gulf Stream and Agulhas Return Current in winter. *J. Climate*, **33**, 9083–9101, https://doi.org/10.1175/JCLI-D-19-0948.1.

Matsuno, T., 1966: Quasi-geostrophic motions in the equatorial area. *J. Meteor. Soc. Japan*, **44**, 25–43, https://doi.org/10.2151/jmsj1965.44.1_25.

Mears, C. A., J. Scott, F. J. Wentz, L. Ricciardulli, S. M. Leidner, R. Hoffman, and R. Atlas, 2019: A near-real-time version of the Cross-Calibrated Multiplatform (CCMP) ocean surface wind velocity data set. *J. Geophys. Res. Oceans*, **124**, 6997–7010, https://doi.org/10.1029/2019JC015367.

Minobe, S., A. Kuwano-Yoshida, N. Komori, S.-P. Xie, and R. J. Small, 2008: Influence of the Gulf Stream on the troposphere. *Nature*, **452**, 206–209, https://doi.org/10.1038/nature06690.

——, M. Miyashita, A. Kuwano-Yoshida, H. Tokinaga, and S.-P. Xie, 2010: Atmospheric response to the Gulf Stream: Seasonal variations. *J. Climate*, **23**, 3699–3719, https://doi.org/10.1175/2010JCLI3359.1.

Nakamura, H., T. Sampe, Y. Tanimoto, and A. Shimpo, 2004: Observed associations among storm tracks, jet streams and midlatitude oceanic fronts. *Earth's Climate: The Ocean-Atmosphere Interaction*, *Geophys. Monogr.*, Vol. 147, Amer. Geophys. Union, 329–346, https://doi.org/10.1029/147GM18.

Nelson, J., and R. He, 2012: Effect of the Gulf Stream on winter extratropical cyclone outbreaks. *Atmos. Sci. Lett.*, **13**, 311–316, https://doi.org/10.1002/asl.400.

O'Neill, L. W., D. B. Chelton, and S. K. Esbensen, 2003: Observations of SST-induced perturbations of the wind stress field over the Southern Ocean on seasonal timescales. *J. Climate*, **16**, 2340–2354, https://doi.org/10.1175/2780.1.

——, T. Haack, D. B. Chelton, and E. Skyllingstad, 2017: The Gulf Stream convergence zone in the time-mean winds. *J. Atmos. Sci.*, **74**, 2383–2412, https://doi.org/10.1175/JAS-D-16-0213.1.

——, ——, ——, and ——, 2018: Reply to comments on "The Gulf Stream convergence zone in the time-mean winds." *J. Atmos. Sci.*, **75**, 2151–2153, https://doi.org/10.1175/JAS-D-18-0044.1.

Parfitt, R., and A. Czaja, 2016: On the contribution of synoptic transients to the mean atmospheric state in the Gulf Stream region. *Quart. J. Roy. Meteor. Soc.*, **142**, 1554–1561, https://doi.org/10.1002/qj.2689.

——, and H. Seo, 2018: A new framework for near-surface wind convergence over the Kuroshio Extension and Gulf Stream in wintertime: The role of atmospheric fronts. *Geophys. Res. Lett.*, **45**, 9909–9918, https://doi.org/10.1029/2018GL080135.

——, and Y.-O. Kwon, 2020: The modulation of Gulf Stream influence on the troposphere by the eddy-driven jet. *J. Climate*, **33**, 4109–4120, https://doi.org/10.1175/JCLI-D-19-0294.1.

——, A. Czaja, S. Minobe, and A. Kuwano-Yoshida, 2016: The atmospheric frontal response to SST perturbations in the Gulf Stream region. *Geophys. Res. Lett.*, **43**, 2299–2306, https://doi.org/10.1002/2016GL067723.

——, ——, and H. Seo, 2017: A simple diagnostic for the detection of atmospheric fronts. *Geophys. Res. Lett.*, **44**, 4351–4358, https://doi.org/10.1002/2017GL073662.

Plougonven, R., A. Foussard, and G. Lapeyre, 2018: Comments on "The Gulf Stream convergence zone in the time-mean winds." *J. Atmos. Sci.*, **75**, 2139–2149, https://doi.org/10.1175/JAS-D-17-0369.1.

Reeder, M. J., T. Spengler, and C. Spensberger, 2021: The effect of sea surface temperature fronts on atmospheric frontogenesis. *J. Atmos. Sci.*, **78**, 1753–1771, https://doi.org/10.1175/JAS-D-20-0118.1.

Samelson, R. M., L. W. O'Neill, D. B. Chelton, E. D. Skyllingstad, P. L. Barbour, and S. M. Durski, 2020: Surface stress and atmospheric boundary layer response to mesoscale SST structure in coupled simulations of the Northern California Current System. *Mon. Wea. Rev.*, **148**, 259–287, https://doi.org/10.1175/MWR-D-19-0200.1.

Schneider, N., 2020: Scale and Rossby number dependence of observed wind response to ocean-mesoscale sea surface temperatures. *J. Atmos. Sci.*, **77**, 3171–3192, https://doi.org/10.1175/JAS-D-20-0154.1.

——, and B. Qiu, 2015: The atmospheric response to weak sea surface temperature fronts. *J. Atmos. Sci.*, **72**, 3356–3377, https://doi.org/10.1175/JAS-D-14-0212.1.

Seo, H., and Coauthors, 2022: Ocean mesoscale and frontal-scale ocean–atmosphere interactions and influence on large-scale climate: A review. *J. Climate*, **36**, 1981–2013, https://doi.org/10.1175/JCLI-D-21-0982.1.

Shimada, T., and S. Minobe, 2011: Global analysis of the pressure adjustment mechanism over sea surface temperature fronts using AIRS/Aqua data. *Geophys. Res. Lett.*, **38**, L06704, https://doi.org/10.1029/2010GL046625.

Siqueira, L., and B. P. Kirtman, 2016: Atlantic near-term climate variability and the role of a resolved Gulf Stream. *Geophys. Res. Lett.*, **43**, 3964–3972, https://doi.org/10.1002/2016GL068694.

Skyllingstad, E. D., S. P. de Szoeke, and L. W. O'Neill, 2019: Modeling the transient response of tropical convection to mesoscale SST variations. *J. Atmos. Sci.*, **76**, 1227–1244, https://doi.org/10.1175/JAS-D-18-0079.1.

Small, R. J., R. A. Tomas, and F. O. Bryan, 2014: Storm track response to ocean fronts in a global high-resolution climate model. *Climate Dyn.*, **43**, 805–828, https://doi.org/10.1007/s00382-013-1980-9.

Sobel, A. H., and J. D. Neelin, 2006: The boundary layer contribution to intertropical convergence zones in the quasi-equilibrium tropical circulation model framework. *Theor. Comput. Fluid Dyn.*, **20**, 323–350, https://doi.org/10.1007/s00162-006-0033-y.

Solman, S. A., and I. Orlanski, 2010: Subpolar high anomaly preconditioning precipitation over South America. *J. Atmos. Sci.*, **67**, 1526–1542, https://doi.org/10.1175/2009JAS3309.1.

Soster, F., and R. Parfitt, 2022: On objective identification of atmospheric fronts and frontal precipitation in reanalysis datasets. *J. Climate*, **35**, 4513–4534, https://doi.org/10.1175/JCLI-D-21-0596.1.

Spall, M. A., 2007: Midlatitude wind stress–sea surface temperature coupling in the vicinity of oceanic fronts. *J. Climate*, **20**, 3785–3801, https://doi.org/10.1175/JCLI4234.1.

Stevens, B., J. Duan, J. C. McWilliams, M. Münnich, and J. D. Neelin, 2002: Entrainment, Rayleigh friction, and boundary layer winds over the tropical Pacific. *J. Climate*, **15**, 30–44, https://doi.org/10.1175/1520-0442(2002)015<0030:ERFABL>2.0.CO;2.

Sullivan, P. P., and J. C. McWilliams, 2022: Atmospheric boundary layers over an oceanic eddy. *J. Atmos. Sci.*, **79**, 2601–2620, https://doi.org/10.1175/JAS-D-22-0019.1.

——, ——, J. C. Weil, E. G. Patton, and H. J. S. Fernando, 2020: Marine atmospheric boundary layers above heterogeneous SST: Across-front winds. *J. Atmos. Sci.*, **77**, 4251–4275, https://doi.org/10.1175/JAS-D-20-0062.1.

——, ——, ——, ——, and ——, 2021: Marine atmospheric boundary layers above heterogeneous SST: Alongfront winds. *J. Atmos. Sci.*, **78**, 3297–3315, https://doi.org/10.1175/JAS-D-21-0072.1.

Takatama, K., S. Minobe, M. Inatsu, and R. J. Small, 2015: Diagnostics for near-surface wind response to the Gulf Stream in a regional atmospheric model. *J. Climate*, **28**, 238–255, https://doi.org/10.1175/JCLI-D-13-00668.1.

Tiedtke, M., 1989: A comprehensive mass flux scheme for cumulus parameterization in large-scale models. *Mon. Wea. Rev.*, **117**, 1779–1800, https://doi.org/10.1175/1520-0493(1989)117<1779:ACMFSF>2.0.CO;2.

Tokinaga, H., Y. Tanimoto, S.-P. Xie, T. Sampe, H. Tomita, and H. Ichikawa, 2009: Ocean frontal effects on the vertical development of clouds over the western North Pacific: In situ and satellite observations. *J. Climate*, **22**, 4241–4260, https://doi.org/10.1175/2009JCLI2763.1.

Vannière, B., A. Czaja, H. Dacre, and T. Woollings, 2017a: A "cold path" for the Gulf Stream–troposphere connection. *J. Climate*, **30**, 1363–1379, https://doi.org/10.1175/JCLI-D-15-0749.1.

——, ——, and H. F. Dacre, 2017b: Contribution of the cold sector of extratropical cyclones to mean state features over the Gulf Stream in winter. *Quart. J. Roy. Meteor. Soc.*, **143**, 1990–2000, https://doi.org/10.1002/qj.3058.

Wenegrat, J. O., and R. S. Arthur, 2018: Response of the atmospheric boundary layer to submesoscale sea-surface temperature fronts. *Geophys. Res. Lett.*, **45**, 13 505–13 512, https://doi.org/10.1029/2018GL081034.

Wills, S. M., D. W. J. Thompson, and L. M. Ciasto, 2016: On the observed relationships between variability in Gulf Stream sea surface temperatures and the atmospheric circulation over the North Atlantic. *J. Climate*, **29**, 3719–3730, https://doi.org/10.1175/JCLI-D-15-0820.1.

Xie, S.-P., M. Ishiwatari, H. Hashizume, and K. Takeuchi, 1998: Coupled ocean-atmospheric waves on the equatorial front. *Geophys. Res. Lett.*, **25**, 3863–3866, https://doi.org/10.1029/1998GL900014.